Geophys. J. Int. (2002) **151,** 689–709

The 3D electromagnetic response of the Earth to ring current and auroral oval excitation

Ikuko Fujii[1] and Adam Schultz[2]

[1]*Kakioka Magnetic Observatory, Japan Meteorological Agency, Kakioka* 595, *Yasato-machi, Niihari-gun, Ibaraki,* 315-0116, *Japan. E-mail: fji@kakioka-jma.go.jp*
[2]*Earth Science Department, Cardiff University,* PO Box 914, *Cardiff,* CF10 3YE, *UK*

Accepted 2002 May 8. Received 2002 May 2; in original form 2001 February 9

SUMMARY

We report on a new compilation of functions representing the geoelectromagnetic response of the Earth's mantle. The *c* response functions and newly defined *d* response functions, the latter of which constitutes a sensitive indicator of lateral heterogeneities in conductivity, were estimated for periods from 5 to 106.7 days. The spatial coverage and statistical quality of these response-function estimates were improved over previous compilations, in part by making use of a newly assembled global catalogue of magnetic observatory hourly mean values, and by applying a statistically robust form of empirical orthogonal function (EOF) analysis. The EOF results suggest that for periods longer than 5 days, the geomagnetic field variation can be represented predominantly by a single eigenmode. We have identified that the primary-source fields of the dominant mode consist of two current systems in the same direction: an equatorial ring current in the magnetosphere, and two conjugate auroral oval ring currents in the ionosphere. The influence of the auroral current system is seen at surprisingly low latitudes, 40° and 50° for the vertical and northern components, respectively, which results in non-negligible bias on the conventional *c* response at high latitudes. A preliminary correction of the auroral current effect has been made on the *c* and *d* responses obtained for data from 55 and 52 observatories, respectively, at latitudes from −60° to 60°. We also present a set of approximate equivalent internal (mantle) electrical current distributions that prove a useful indicator of the presence of deep Earth heterogeneities. These new sets of electromagnetic information will increase the resolving power of 3D distribution of electrical conductivity in the Earth's mantle.

Key words: electrical conductivity, electromagnetic induction, geomagnetic variation, ionosphere, magnetosphere, statistical methods.

1 INTRODUCTION

The geoelectromagnetic spectrum arises from the superposition of multiple external source fields with induced fields set up inside the conducting Earth. The electrical conductivity of the materials comprising the Earth's interior is dependent upon temperature, composition (e.g. Fe content), state (e.g. partial fraction of melt), and the presence of volatiles (Karato 1990; Shankland & Duba 1990; Bai & Kohlstedt 1992; Shankland *et al.* 1993; Hirsh *et al.* 1993). It has been established that the electrical conductivity of the Earth's mantle varies radially (e.g. Lahiri & Price 1939; Banks 1969) and a body of evidence has been assembled that points to significant lateral heterogeneity as well (e.g. Schultz & Larsen 1990; Lizarralde *et al.* 1995). Our goal is to determine the electromagnetic response of such a 3D Earth to external excitation, and to use that response to constrain the internal conductivity distribution. This will shed light on the pattern of convection within, and the cycling of lithospheric materials through the mantle. Geoelectromagnetically-induced signals recorded on the Earth's surface provide an avenue by which such mantle conductivity variations may be determined.

We extract the signal due to the primary-source field from the background variations. This is used to measure the response of the heterogeneous Earth to the statistically stationary component of the external excitation. We consider here the problem of global-scale electromagnetic induction in the Earth's mantle by long-period geomagnetic field variations (from 5 to 106.7 days). This signal comes primarily from variations in the magnetospheric equatorial ring current and, particularly at higher geomagnetic latitudes, the ionospheric auroral oval current systems. Non-stationary sources are superimposed on these signals, which we consider as statistical noise.

A new global catalogue of geomagnetic observatory hourly mean values was assembled in order to provide richer geographical and temporal coverage of geomagnetic field variations than available

previously. We have applied empirical orthogonal functional (EOF) analysis (e.g. Lorenz 1956; Anderson 1963; Wallace & Dickinson 1972; Egbert 1997) to extract spatially and temporally coherent geomagnetic field structure from the partially incoherent geomagnetic variations background contained within this catalogue. Such a background arises from the amalgamation of signals from multiple magnetospheric and ionospheric electrical current systems. Statistically robust methods were used to reduce bias from non-stationary and discordant data. In carrying out this work, we have gained new insight into the effects of induction due to the auroral oval current systems. We have for the first time in deep mantle induction studies included these auroral systems simultaneously with the source fields associated with the magnetospheric equatorial ring current.

The result of these calculations is a new set of globally distributed electromagnetic response functions in two forms. The first is a conventional scaled ratio of local vertical and horizontal magnetic field components (the local 'c' response), and the second is the scaled ratio of two local orthogonal magnetic-field components (the local 'd' response). This second form has particular value in interpreting the electromagnetic response of a 3D Earth to external excitation, if contributions from non zonal long-period variations can be ruled out. Finally, we have calculated a set of (approximate) equivalent internally induced electrical current systems. These provide a convenient means of visualizing the diversion of currents by anomalous resistive and conductive zones within the Earth's interior.

This collection of response functions and equivalent current distributions is presently being used in an inverse mapping project that employs a newly-developed forward solution for Maxwell's equations in a 3D heterogeneous spherical Earth (Uyeshima & Schultz 2000; Toh *et al.* submitted). We shall report in a subsequent publication on a 3D model of the electrical conductivity distribution within the Earth's mantle that is being assembled from the inversion of the response functions reported here.

2 GLOBAL ELECTROMAGNETIC RESPONSE FUNCTIONS

Schmucker's (1970) scalar response c provides a conventional means of estimating the electromagnetic response of the conducting Earth,

$$c(\omega) = \frac{-B_r(\omega)}{\nabla_h \cdot \mathbf{B}_h(\omega)}, \tag{1}$$

where B_r and $\mathbf{B}_h$ are the radial and horizontal components of the geomagnetic field, respectively, and ω denotes the angular frequency. The simplifying assumption is typically made that the magnetospheric equatorial ring current is the primary source of the geomagnetic variations within the period band of approximately 2 days to 2 years (e.g. Banks 1969; Schultz & Larsen 1987). This source arises from the relaxation phase of $D_{\rm st}$ variations. It is this period band in which the induced signal contains greatest sensitivity to variations in upper to mid-mantle conductivity. Until relatively recently it has been generally assumed that the electrical conductivity structure of the mantle varies only with radial depth (e.g. Olsen 1998, 1999; Schmucker 1999b). Under these assumptions the geomagnetic field is approximated by a dipole field, and the c response may be given entirely by the ratios of local magnetic field components,

$$c(\omega) = \frac{R \tan\theta}{2} \frac{B_r(\omega)}{B_\theta(\omega)}, \tag{2}$$

where R and θ denote the radius of the Earth and the geomagnetic colatitude, respectively. Since the term $\tan\theta$ compensates for the spatial structure of the source, the c response due to zonal excitation should be the same everywhere on the surface of such a 1D Earth.

The practical consequence of calculating c entirely from magnetic field components known only at a specific point on the Earth's surface (eq. 2) is that no knowledge is required of the horizontal derivatives of the field. This is in contrast to the global c response defined in (eq. 1). Given the sparse and irregular distribution of observatory sites (see Section 2 below), it is often difficult to determine horizontal field gradients accurately.

In contrast to this idealised 1D view of deep Earth conductivity structure, reports on significant lateral variations of the c response have been accumulating (e.g. Schultz & Larsen 1987; Lizarralde *et al.* 1995; Neal *et al.* 2000), demonstrating that the mantle has a multi-dimensional structure. This is not surprising, given the wealth of evidence in support of geophysically-detectable lateral variations in material properties, mainly thus far from seismology (e.g. Boschi & Dziewonski 1999; Van Heijst & Woodhouse 1999; Fukao 1992). It would be curious to support a view of the mantle that could exhibit such heterogeneities in elastic properties whilst simultaneously failing to require significant heterogeneities in electrical conductivity.

During the past decade, the local c response has been the primary source of information about deep lateral variations in electrical conductivity. An investigation of the sensitivity of c to such lateral heterogeneities was carried out as part of the construction of the first 3D inverse model of deep mantle conductivity (Schultz & Pritchard 1999). This has been followed up by recent and more detailed numerical simulations making use of a new staggered grid 3D finite difference solution for electromagnetic induction in a heterogeneous sphere (Uyeshima & Schultz 2000; Toh *et al.* submitted).

Fig. 1 displays the anomalous part of the c response of a heterogeneous spherical Earth comprising a uniformly conducting mantle in which a small conductive sphere is embedded. The result shown was obtained using the method of Uyeshima & Schultz (2000), and is one of a range of model parametrization investigated. The small diameter of the sphere whose response is displayed in Fig. 1 (400 km) was chosen to represent a geodynamically interesting target of minimally resolvable size. By exposing such a model to zonally symmetric source field excitation, both zonal and meridional anomalous fields arise. The broadscale and zonal nature of the source results in only a weak meridional response. Galvanic charges are set up on the surface of the embedded sphere, but these are of modest magnitude. The resulting anomaly in c (eq. 2) is comparably small, with a maximum perturbation at the Earth's surface of approximately ± 7 per cent. This is of similar magnitude to the confidence limits found in published catalogues of c responses (e.g. Schultz & Larsen 1987). We conclude that such small but geodynamically significant targets will, under zonally symmetric source excitation, lie just at the threshold of detectibility of local c responses. There may be other geodynamic targets capable of generating larger anomalous c responses, but this small and more challenging target provides a useful gauge of the sensitivity of alternative response function forms to 3D effects.

The relative insensitivity of c to the inhomogeneity of the mantle revealed by this and other calculations suggests that c may provide a fairly robust view of the underlying (local) depth dependent variations in mantle conductivity. Conversely, inversion of the c response alone may be insufficient to resolve the expected deep lateral variations adequately. This concern has lead to proposals for new global response functions forms (e.g. the ζ response of Zhang & Schultz 1992). To increase the sensitivity to lateral inhomogeneities, knowledge of the geomagnetic field as well as either the geoelectric field (e.g. magnetotellurics), or the spatial derivatives of the magnetic

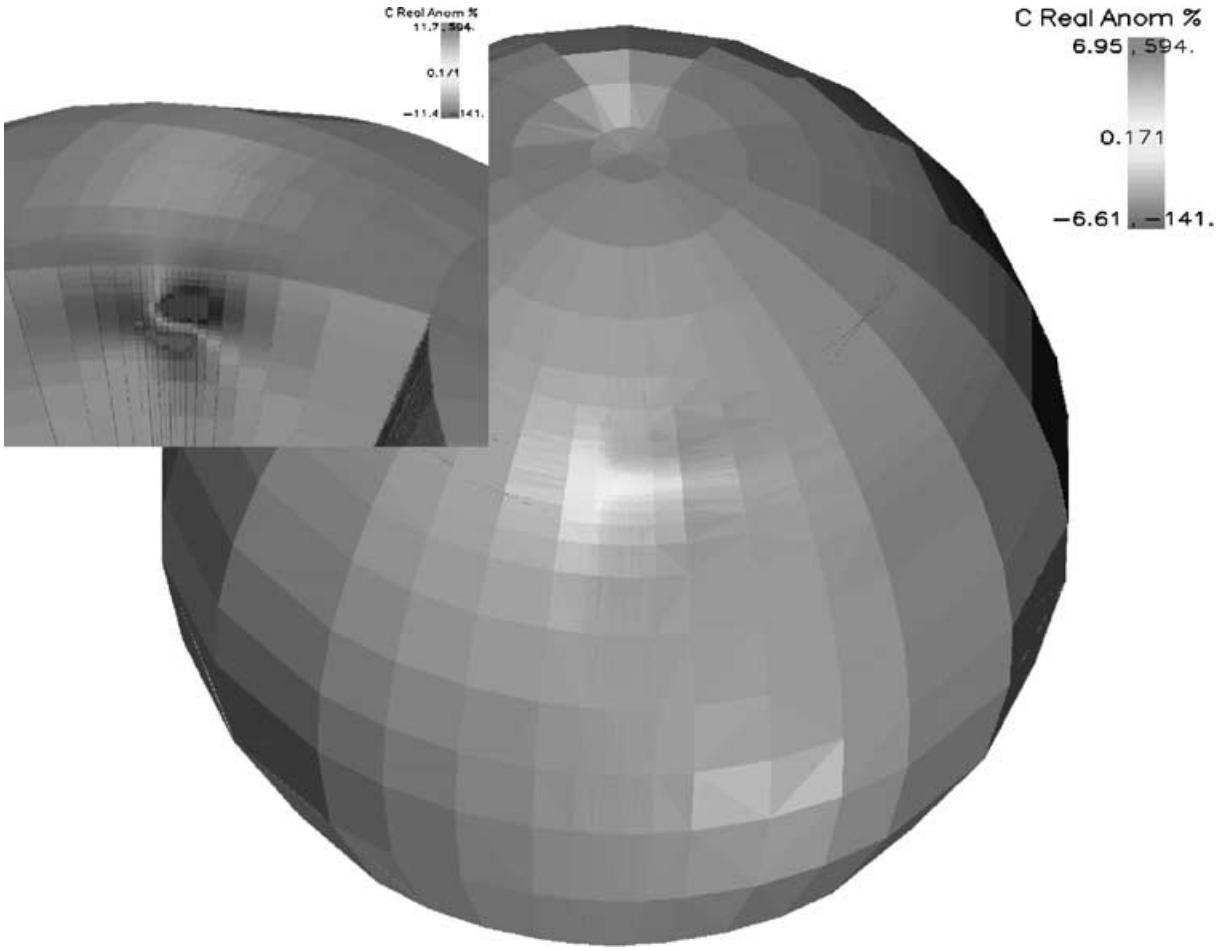

Figure 1. Anomalous part of c response of a 3D numerical model (Uyeshima & Schultz 2000) of a heterogeneous spherical earth comprising a uniformly conducting mantle of 1 S m^{-1} in which is embedded at a depth of 400 km and at a central latitude of 45° a conductive sphere of 10 S m^{-1} and radius 200 km. The model earth is excited by a source current of period 25 d, and with P_1^0 form, representing an equatorial ring current at a radius of 10 R. The quantity displayed is the $c_{\text{anom}} = c_{3\text{D}} - c_{1\text{D}}$, where the first quantity represents the c response of the 3D model, and the second represents the c response of a uniformly conductive homogeneous mantle of 1 S m^{-1}. Both models are terminated by a perfect conductor at the CMB. The total anomalous part of the c response seen at the earth's surface is seen to be ≈±7 per cent. Within the earth's interior (inset), in the vicinity of the anomalous spherical inclusion, the peak anomaly is ≈±12 per cent.

field (ζ response) is required. Long term observations of the geoelectric field are rare in comparison to those of the geomagnetic field (e.g. Egbert *et al.* 1992; Schultz *et al.* 1993; Bahr *et al.* 1993; Lizarralde *et al.* 1995) although where available magnetotelluric information has been used to good effect in examining deep regional conductivity.

The alternative of using both the magnetic field and its horizontal derivatives has proved more problematic. Some workers report success in using spectral methods (spherical harmonic analysis, spherical cap analysis, etc.) to estimate the horizontal derivatives from the global distribution of geomagnetic observations as required by eq. (1) (e.g. Olsen 1998, 1999). Our investigations into determination of accurate response function forms suggest a more pessimistic outcome in the context of imaging the 3D variations of mantle properties. The problem stems from the geographically sparse and irregular distribution of the magnetic observatory network. This spatial distribution makes it impossible to determine horizontal field gradients sufficiently well so that response function estimates of acceptable accuracy may be obtained within the period band of 2 days to 2 years. It is only within the densely instrumented European and Far Eastern observatory networks that response functions can be estimated with confidence limits smaller than 10 per cent. A similar conclusion can be inferred from Banks & Ainsworth (1992).

The difficulty in extracting reliable estimates of horizontal field gradients impedes our efforts to make use of less restrictive forms (with regard to the source structure) of c (eq. 1) or alternative response functions requiring spatial gradient information (e.g. ζ). In the present work and under the dipole source assumption, c can be computed independently at each observatory and will reflect primarily the effects of regional 1D structure. We use this information as one constraint on the lateral heterogeneity of the mantle.

We propose a scalar response function form complementary to c. The d response is defined:

$$d = \frac{R \sin\theta}{2} \frac{B_\phi}{B_\theta}. \tag{3}$$

The d response is designed to extract information on 3D inhomogeneities in conductivity whilst retaining the site independent properties of the local c response. The ϕ component of the geomagnetic field is zero if the mantle is 1D and the source is zonal. Therefore, non-zero values of d arise under such excitation only in the presence of lateral conductivity heterogeneities. This effect is illustrated in

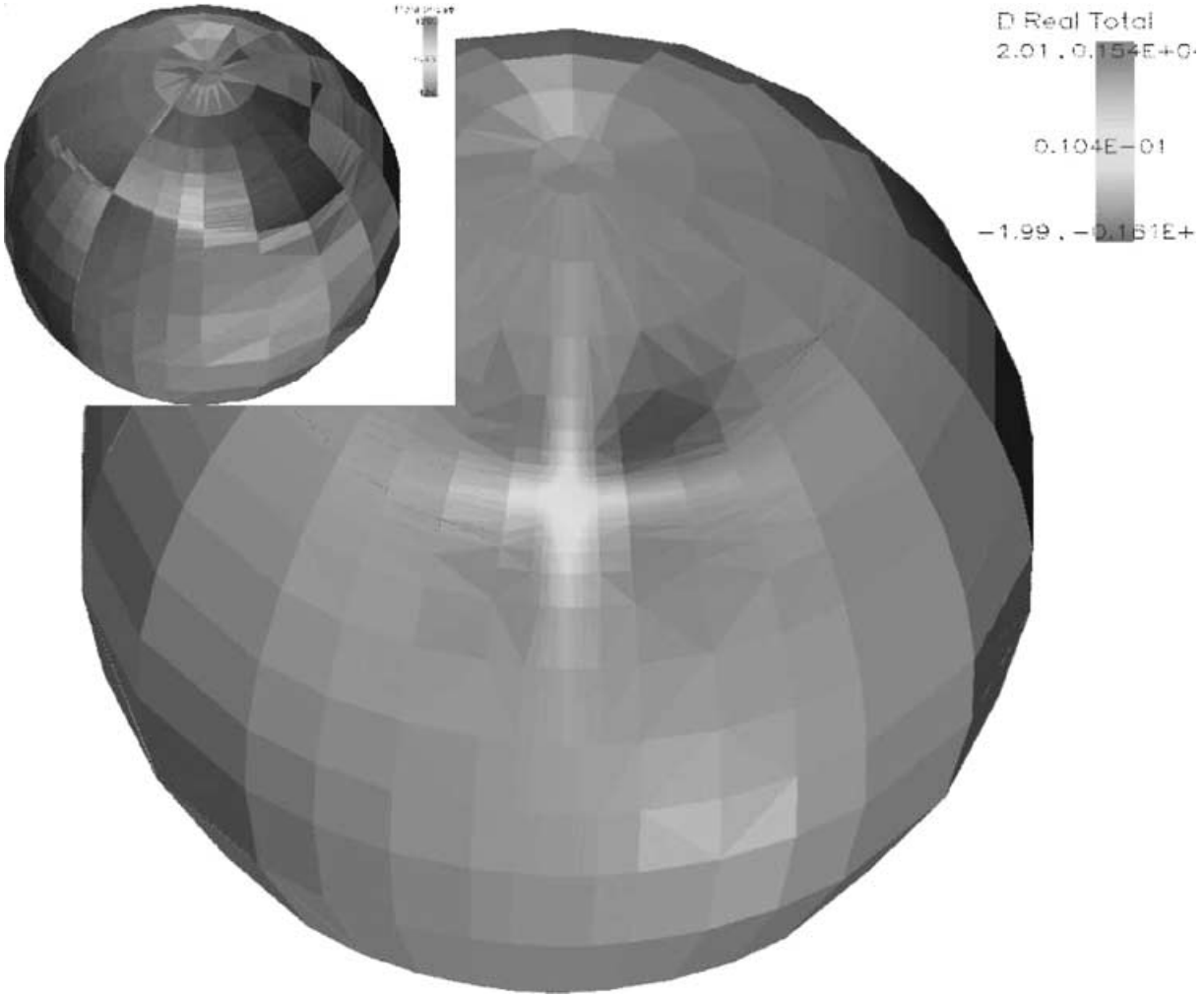

Figure 2. The *d* response of the same 3D numerical model and for the same source configuration and period whose *c* response was shown in Fig. 1. In contrast to the *c* response, *d* is undefined for a 1D earth under zonal excitation The *d* response indicates clearly the presence of the 3D heterogeneity embedded within an otherwise uniform model mantle. The strong 3D signature is seen best in the phase of the ϕ component of *B*. This is shown in the inset. For a 1D earth under zonal excitation, B_ϕ is identically zero.

Fig. 2. In the presence of zonal source field excitation, secondary magnetic fields are set up in the region of the small embedded conductive sphere, with a particularly strong signature in B_ϕ. The inset in Fig. 2 shows that it is the phase of this component that is most greatly affected by the presence of the target sphere. Where the conventional local *c* response (eq. 2) is insensitive to the phase of B_ϕ, the local *d* response is influenced strongly. By considering *c* and *d* responses in aggregate, and also including additional information on equivalent internal current systems (described below in Section 8), we believe that significant improvements can be made to the resolving power of inverse models of 3D mantle conductivity.

3 DATA AND PRE-PROCESSING

We have constructed a database of hourly mean values of the geomagnetic field from 1901 to 1995 that encompasses a set of 241 observatories. The data sources are the British Geological Survey, the Chambon la Foret Observatory, the collections of Gupta and Winch, the Geological Survey of Canada, the Intermagnet programme, World Data Centers A (NGDC), B, C1 and C2. The data distribution in time and space domains is shown in Fig. 3. Observatories used in the present study are marked with solid circles and others are marked with solid triangles.

In order to carry out initial spectral analysis of these data through Fast Fourier transformation, it is necessary to identify and remove embedded gaps in the data. Data found to be outliers (clearly drawn from probability distributions subsidiary to the main probability density function (PDF)) and data gaps shorter than 1.5 days were replaced and filled according to the iterative and statistically robust multivariate transfer function approach of Zhang & Schultz (1990). For data from mid- and low latitude geomagnetic observatories, the procedure followed has identified and replaced outliers of scale larger than 100 nT. For data from higher latitude observatories, the larger RMS amplitude of geomagnetic time variations there has required us to set the threshold higher, approximately a few hundreds of nT. These initial gap predictions serve as pilot estimates that will be subsequently refined during the Empirical Orthogonal Function estimation procedure described in Section 4.

We have corrected 510 baseline shifts, reversed the sign of 16 magnetic observatory components, and corrected incorrect dates for 4 components. Data of two observatories which showed apparently non-physical values were removed from the data set.

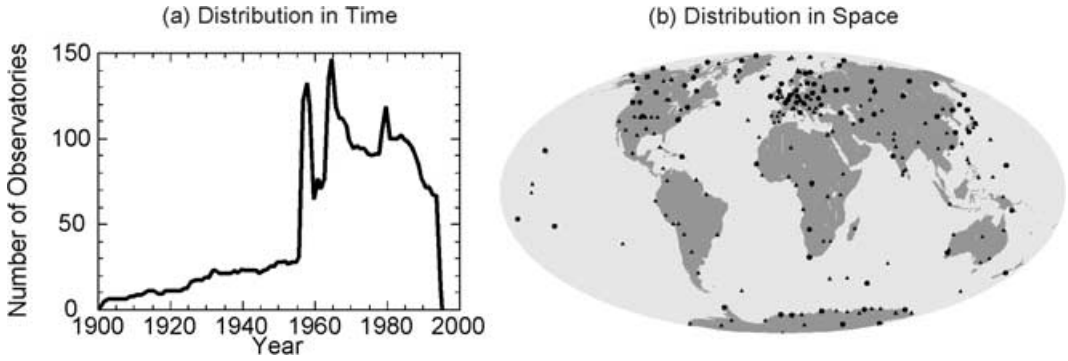

Figure 3. Distribution of geomagnetic observatories from 1900 to 1995 in both time (a) and space (b). Solid circles show the locations of 84 observatories used in the present study. The remaining 157 observatories are marked with solid triangles.

The hourly vector magnetic field values from 1957 to 1995 were used in this study because of the availability of data from a particularly large number of observatories during this time period. The solar quiet variations S_q and its harmonics, and 7 major oceanic tides, if detectable, were removed from the hourly data set by using a robust least-squares fitting method. The hourly data of horizontal force (H), declination (D) and downward positive vertical component (Z) at 84 observatories were lowpass filtered with a non-recursive digital filter of 48 hour cut-off period by Hamming (1977) and resampled into daily values. The Hamming filter was chosen because of a smooth characteristic curve in the frequency domain and zero-phase shift. The annual and semiannual signals were removed from the daily values in the same manner. The north (B_x) and east (B_y) field components in geomagnetic coordinates were then computed from the H and D components in geographic coordinates. Locations of the geomagnetic pole for 1957–1995 were obtained from two dipole components of the IGRF model (Barton 1997). The secular motion of the pole is not relevant because this rate is much slower than the period range of interest in the present study. Finally, the mean and linear trend were removed from B_x, B_y, and B_z (i.e. Z) from entire time-series.

The daily data set was highpass filtered with a Hamming filter of 128 day cut-off period and 387 data values filter length. Embedded data gaps of duration longer than 1.5 days but shorter than the cut-off period were filled initially by projecting the previous and subsequent data segments (each of 15 data values length) through an autoregressive (AR) filter. This in-filling process was required to prevent data gaps from destroying the effectiveness of high pass filtration. These filled values were subsequently replaced by values obtained after subsequent processing (see Section 4.2 below). The highpass filtered daily values were used for analysis at periods from 2 to 42.7 days.

The daily data set was also lowpass filtered with a Hamming filter of 10 day cut-off period, and resampled into 5 day values. Any remaining gaps shorter than 10 days were filled by projecting the 15 preceding and 15 subsequent data through an AR filter. The 5 day values were highpass filtered in the same manner as the daily data set and were used for analysis at periods from 10 to 106.7 days.

4 EMPIRICAL ORTHOGONAL FUNCTIONS

The ultimate goal of electromagnetic induction imaging (EMI) methods is to reveal the spatial distribution of electrical conductivity in the Earth's interior, and to use such 'images' to constrain Earth parameters of geodynamic interest. To do this usually requires estimating a meaningful set of electromagnetic response functions that can be subsequently inverted for conductivity structure. For this to be successful, the spatial structure of the external source current systems must be established as part of the response function estimation process, or alternatively, the part of the external source that is consistent with an *a priori* structure must be extracted from the more complicated background.

Most efforts to determine the lateral variations in the conductivity of the deep mantle have made use of response functions found to be consistent with a dipolar ring current source and an underlying regional (approximately) 1D conductivity structure (e.g. Schultz & Larsen 1987). This has imposed a serious limitation on the geographical scope of deep EM response functions. Data from the majority of observatories are found to violate one or both of the *a priori* assumptions. This limitation has greatly impeded progress in applying EMI methods to investigations of global-scale mantle geodynamics.

Spherical harmonic analysis (SHA) is the conventional means by which the spatial structure of the geomagnetic field may be decomposed into a set of geographical basis functions. SHA may be used to extract the Gauss coefficients of the field, and thereby to separate internal induced fields from external source fields (Gauss 1838). Unfortunately, SHA suffers severe aliasing effects when confronted with a sparse and uneven distribution of observatory sites. The primarily land-based and northern hemisphere weighted global observatory distribution leads to inaccurate estimates of SHA coefficients (e.g. Schmucker 1999a). The application of regularization methods can damp some of the more egregious consequences of applying SHA to such uneven observatory distributions (e.g. Schultz & Zhang 1994), but the spatial gradients extracted from the resulting spherical harmonic coefficients remain poorly constrained. We have found in practise that given the existing observatory distribution, such conventional methods cannot be used to estimate accurate and meaningful large-scale EM response functions sensitive to the 3D variations of electrical conductivity in the Earth's mantle. We have found it necessary to investigate an alternative approach.

We have developed an iterative and statistically robust multivariate scheme using Empirical Orthogonal Functions (cf. Egbert 1997) (hereafter EOF) to examine the spatial characteristics of the geomagnetic field. EOFs, also known as the 'principal component method', were used here to detect induced features of the irregularly-sampled (in space and time) geomagnetic field. Statistically robust estimation methods (Chave *et al.* 1987; Chave & Thomson 1989) are required in order to accommodate data drawn from a primary distribution that have been contaminated by 'noise' drawn from other distributions. Typically, such outliers result in abnormally long or short tails for an

otherwise Gaussian distribution, although no restriction to this specific situation is made here. In our scheme, which differs from that used by Egbert, the EOF eigenvectors were obtained by inverting a covariance matrix directly, the standard errors used in the analysis are approximated by summing the higher order modes of the EOF, and a robust procedure was applied to the data in the time domain as well as in the frequency domain. We shall describe our scheme in the next 6 subsections.

4.1 Basis of the EOF procedure

The data comprise in total K time-series components at P observation sites where $K = 3P - G$, where G is the number of components either totally missing from the data set, or with too many embedded gaps to be included. The coefficients of the EOF are obtained in the frequency domain by a section averaging procedure. The kth time-series component of the data set $(x_k(t))$ is divided into N time sections, each of which overlaps its neighbours by 50 per cent. To minimize leakage of spectral power from adjoining and distant frequencies (periodogram bias) we apply a time-bandwidth product 1 (i.e. a 'π') prolate spheroidal taper function (Slepian 1978) to each time section according to the method of Thomson (1982). Fourier transformation of the tapered time-series sections results in N sets of complex spectra $\mathbf{x}$ for each of the K time-series components.

The following conventions on naming subscripts holds for the discussion below: $i = 1, 2, \ldots, N$ identify time-series sections; $k, l = 1, 2, \ldots, K$ identify the components and the observatories from which time-series segments are drawn; $m, n = 1, 2, \ldots, M$ identify the eigenvalues and associated eigenvectors.

For a given time-series section i of length T (this is held constant for all time-series sections) and angular frequency $\omega_p = 2\pi p/T$, an EOF is obtained that expresses a linear relationship between the Fourier coefficients of the K time-series components:

$$x_{ki} = \sum_{m=1}^{M} u_{km}\alpha_{mi} + \varepsilon_{ki}, \tag{4}$$

or

$$\mathbf{x}_i = \mathbf{U}\mathbf{a}_i + \mathbf{e}_i, \tag{4'}$$

where u_{km} is the k-th element of a vector $\mathbf{u}_m = (u_{km})^{\mathrm{T}}$. The vectors $\mathbf{u}$ are the column vectors of matrix $\mathbf{U} = (u_{km})$. The set of $\mathbf{u}_m$ denotes the significant EOF modes or principal components, i.e. the set of linear basis functions. The vector $\mathbf{a}_i = (\alpha_{mi})^{\mathrm{T}}$ is the set of coefficients by which the mode vectors are multiplied for a given time section i in order to reproduce the Fourier coefficients vector $\mathbf{x}_i$ for that section.

M denotes the number of significant modes, $M \leq K$. The noise term ε_{ki} is estimated from $M - K$ insignificant modes in this study as

$$\varepsilon_{ki} = \sum_{m=M+1}^{K} u_{km}\alpha_{mi}. \tag{5}$$

If $M = K$ the original Fourier coefficients are reproduced exactly, and $\mathbf{e}_i$ equals zero identically. If $M < K$ the vector $\mathbf{e}_i$ may be non-zero, in which case it contains the portion of the spectral energy found to lie outside the EOF projection through the linear basis functions $\mathbf{u}_m$, i.e. the incoherent 'noise'. The proper choice of M reflects the fact that lower order modes tend to reflect signals of more global scale (high station-to-station coherence). Higher order modes contain more localized signals (lower station-to-station coherence), i.e. local signals cannot explain the cross-spectral patterns of the whole data set. This 'screening' is widely applied in physical oceanographic studies, e.g. Davis (1976) and Preisendorfer & Barnett (1977) propose methods for choosing M. The method to choose M used in this study is described in Section 4.2.

The vector $\mathbf{a}_i$ satisfies the orthogonality condition

$$\sum_{i=1}^{N} \alpha_{mi}^{*} \cdot \alpha_{ni} = \delta_{mn} \sum_{i=1}^{N} |\alpha_{mi}|^2 = \delta_{mn}\lambda_m \tag{6}$$

where $\lambda_m > \lambda_{m-1}$ holds for all m. Eqs (4)–(6) lead to an eigensystem

$$\mathbf{C}\mathbf{u}_m = \lambda_m \mathbf{u}_m \tag{7}$$

where $\mathbf{C}$ is a cross spectral matrix whose lth row and kth column is given by

$$c_{lk} = \frac{1}{N} \sum_{i=1}^{N} x_{li}^{*} x_{ki} \tag{8}$$

Therefore, $\mathbf{u}_m$ and λ_m are the mth eigenvector and eigenvalue of a $K \times K$ Hermitian matrix $\mathbf{C}$. The eigenvectors are orthogonal: $\mathbf{u}_m^{*} \cdot \mathbf{u}_n = \delta_{mn}$. A set of $\mathbf{u}_m$ is obtained by decomposing $\mathbf{C}$. $\mathbf{a}_i$ is computed from $\mathbf{U}$ and $\mathbf{x}_i$:

$$\alpha_i = \mathbf{U}^{*}\mathbf{x}_i. \tag{9}$$

Observing that the orthogonality condition of $\mathbf{u}_m$ implies $\mathbf{U}^{-1} = \mathbf{U}^{*}$, this relation follows readily from eq. (4).

Prior to Fast Fourier Transformation and EOF analysis, we filled embedded gaps in the time-series sections. In Section 3 we referred to the method used to predict missing values from existing data. We used a variation of this method to generate pilot estimates of such missing data, thereby making it possible to determine initial values for the EOFs. For subsequent iterations the predicted values within the data gaps are replaced by new predictions obtained from the latest estimates of the EOF coefficients. The detailed procedure to fill gaps with the EOF coefficients is described in subsection 4.4.

4.2 Normalization by data variance

We consider a simple case for the noise term $\mathbf{e}_i$. Let the uncorrelated noise be drawn from a Gaussian distribution, and let the noise for each field component be independent and identically distributed (*iid*). The uncorrelated noise is then characterized by the variance $\sigma_k, k = 1, \ldots, K$.

The variance σ_k for a given time-series component is not necessarily of the same scale as that for any other component. Geomagnetic variations at high latitudes are generally much larger in amplitude than those at mid and low latitudes. If the signal-to-noise ratios of measurements are comparable at all latitudes, this results in much larger noise variance at high latitudes. Therefore, we normalize the data by the variance,

$$\bar{x}_{ki} = \frac{x_{ki}}{\sigma_k}, \quad (i = 1, K, \ldots, N). \tag{10}$$

Hereafter, variables in the normalized space are written with a bar, i.e. $\bar{\mathbf{x}}_i$. Eqs (4)–(9) are heretofore taken to be in the normalized space.

For the first iteration, σ_k is set to unity. From the second iteration, we evaluate $\mathbf{e}_i$ by setting the number of significant modes (M). The mth mode is categorized as significant (1) if the mth eigenvalue $\bar{\lambda}_m > \beta\bar{\lambda}_1$, where β is an empirical parameter that ranges from 0.01 to 0.05 and is set to reflect amplitude differences among $\bar{\lambda}_m$ so that $\bar{\lambda}_M \gg \bar{\lambda}_{M+1}$, and (2) if any single element of $\bar{\mathbf{u}}_m$ is not significantly larger than others to exclude localized effects.

Rather than calculating the variance in the conventional manner (thereby implicitly assuming the underlying PDF is Gaussian), we

choose instead to compute σ_k from the median absolute deviation (MAD) of ε_{ki}, $i = 1, \ldots, N$. Such an estimate of variance is resistant to bias from deviations from Gaussian distributed noise. The MAD estimate of variance σ_{MAD} is refined in each iteration every time $\bar{\mathbf{u}}_m$ and $\bar{\mathbf{a}}_i$ are re-calculated.

4.3 Robust procedure

Each time σ_k is updated, a soft rejection robust procedure (i.e. outliers are downweighted rather than rejected completely) is applied to the noise term to detect and correct outliers. The normalized noise term $\bar{\varepsilon}_{ki}$ will be drawn from a Gaussian distribution of unit variance and zero mean, if σ_k is estimated correctly. If any noise terms $\bar{\varepsilon}_{ki}$, $k = 1, \ldots, K$ and $i = 1, \ldots, N$, are larger than $2\sigma_{\mathrm{MAD}}$, they are downweighted so $\bar{\varepsilon}_{ki}$ approaches more closely a Gaussian distribution. The updated noise term $\hat{\varepsilon}_{ki}$ in the normalized space is given by

$$\hat{\varepsilon}_{ki} = w_{ki}\bar{\varepsilon}_{ki}, \tag{11}$$

where w_{ki} is a weight function described below. The normalised datum $\bar{\mathbf{x}}_{ki}$ is also updated,

$$\hat{x}_{ki} = \sum_{m=1}^{M} \bar{u}_{km}\bar{\alpha}_{mi} + \hat{\varepsilon}_{ki}. \tag{12}$$

The process to compute $\bar{\mathbf{u}}_m$, $\bar{\mathbf{a}}_i$, M, σ_k, and $\hat{x}_{ki}$ is repeated until no further outliers are detected, or the standard deviation of $\bar{\varepsilon}_{ki}$ (i.e. the root mean square of the prediction residual) <1.2. We chosen 1.2 instead of 1.0 to avoid overfitting the data. The RMS is typically 0.9–1.1 after convergence at the final stage. The resulting $\hat{x}_{ki}$ in the normalized space represents an uncontaminated (i.e. outlier free) Fourier coefficient of the geomagnetic field components for the significant EOF modes only. The $\hat{\varepsilon}_{ki}$ term represents the incoherent 'noise', i.e. the part of the geomagnetic field found to lie outside the projection through the linear basis functions of the EOF.

For the initial three iterations, w_{ki} is set to Huber's influence function (1981),

$$w_{ki} = 1 \quad \text{if } |\bar{x}_{ki}| \le 2\sigma_{\mathrm{MAD}}$$

$$w_{ki} = 2\sigma_{\mathrm{MAD}}/|\bar{x}_{ki}| \quad \text{if } |\bar{x}_{ki}| > 2\sigma_{\mathrm{MAD}}.$$

If the process requires more than three iterations, convergence is accelerated for subsequent iterations by setting w_{ki} to Thomson's influence function (1977) which employs a rapidly decaying exponential function to downweight the data more severely than Huber's, (1981) i.e. $w_{ki} = \exp\{-e^{u_0(|u|-u_0)}\}$, where $u_0 = \Phi^{-1}(1 - 1/N)$, Φ is the cumulative normal distribution function and N is the sample size. Typically, the process converges within three iterations and Thomson weights are rarely used.

4.4 Data gaps in the time domain

Once the uncontaminated Fourier coefficients $\hat{x}_{ki}$ are obtained through the frequency-domain robust procedure described in the previous three subsections, the modified data are transformed back to the time domain to update predictions for the data gaps and detect outliers. This is to prevent a few spurious values in a given time section from destroying the reliability of estimates of the Fourier coefficients for the entire section. The predicted time-series $\tilde{x}_k(t)$ is computed by inverse Fourier transformation of the cleaned values of $\sigma_k\hat{x}_{ki}(\omega)$, $k = 1, \ldots, K$, $i = 1, \ldots, N$ that were obtained in the final iteration of the frequency domain robust procedure. The values within the data gaps are replaced with new predictions. If the residual amplitude $|x_k(t) - \tilde{x}_k(t)|$ is larger than $6\sigma_{\mathrm{MAD}}$ of the residuals, $\tilde{x}_k(t)$ is regarded as an obvious outlier and is replaced with $\tilde{x}_k(t)$. Following this, the Fourier coefficients $\mathbf{x}_{ki}(\omega)$ are updated and the robust EOF procedure of Section 4.1–4.3 is repeated. The whole process of Section 4.1–4.4 is repeated until no further outliers are detected, in practise never more than three times.

4.5 Response functions

Once the uncontaminated data $\hat{x}_{ki}$ are obtained, the spectra of the non-normalized space for the ith time section and k th component are estimated as $\sigma_k\hat{x}_{ki}$ by using the final estimates of σ_k, $\bar{u}_{km}$, $\bar{\alpha}_{mi}$, and $\hat{\varepsilon}_{ki}$ in eq. (12). Suppose the X, Y and Z components of the geomagnetic field for the ith time-series section at a given site are x_{ji}, x_{ki}, and x_{li}, respectively. The time amplifier $\bar{\alpha}_{mi}$ is always common to the three components as shown in eq. 12 and therefore the c response of eq. 2 and d response of eq. 3 is simply estimated for each mode by using each eigenvectors as

$$c = \frac{R\tan\theta}{2}\frac{\sigma_l\bar{u}_{lm}}{\sigma_j\bar{u}_{jm}}, \tag{13}$$

$$d = \frac{R\sin\theta}{2}\frac{\sigma_k\bar{u}_{km}}{-\sigma_j\bar{u}_{jm}}. \tag{14}$$

4.6 EOF confidence limits

Confidence limits on $\mathbf{u}_m$, $\mathbf{a}_i$, and λ_m are computed by the Jackknife method (e.g. Thomson & Chave 1991) after the iterative procedure described above has converged. With σ_k fixed, each ith time section is discarded from the data set in turn and the 'delete-one' EOF modes for the ith time section are obtained by applying the EOF analysis to the remaining $N - 1$ time sections. The variance of the set of delete-one EOF results yields the Jackknife error estimates on the eigenvalues and eigenvectors. For the EM response functions, N sets of the c and d responses are computed by using the first mode of the delete-one eigenvectors, and the variance of these set of delete-one responses gives the confidence limits for the response functions.

5 RESULTS OF THE EOF ANALYSIS

The EOF scheme described in the previous section was applied to the daily and 5-day data sets. There is a trade-off in the response function estimation scheme between the ability to discriminate statistical outliers (longer time-series segments), and the ability to maximize geographical coverage from the greatest number of observatories (shorter time-series segments). We have tested several cases, and for the daily value data set have identified a 15-year segment commencing in 1967 as an optimal trade-off. We included only time-series segments containing less than 40 per cent embedded blank values. For the 5 day values, a 23-year segment commencing in 1964 was used. Time-series segments containing up to 50 per cent embedded gap values were allowed in this case. The total number of time-series involved 79, 79 and 76 for the B_x, B_y and B_z components, respectively, for the daily values, and 77 each for the 5 day values. The FFT window lengths were 128 and 320 days, respectively, and 84 and 51 overlapped time-series sections were used for section averaged spectral analysis.

5.1 Significant modes

The eigenvalues of the first 5 modes in the normalized space for the daily and 5-day values are shown in Fig. 4. The parameter β (see

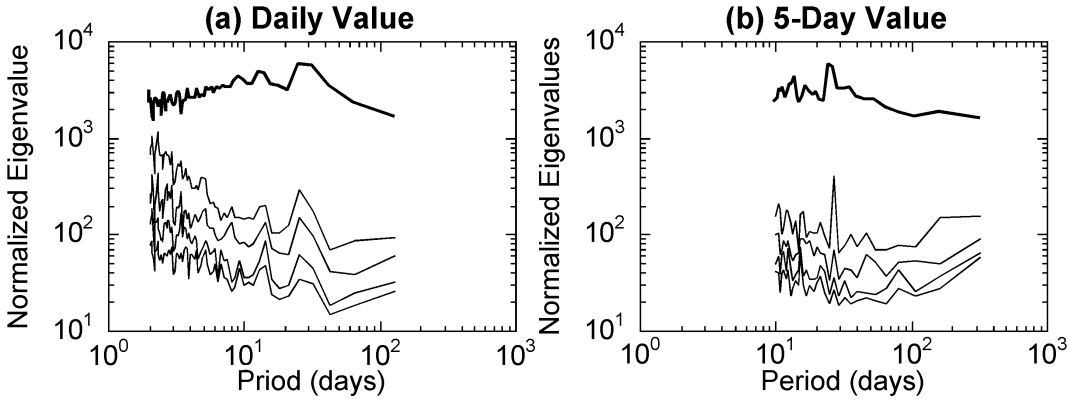

Figure 4. Eigenvalues of the cross spectral matrix **C** for the daily (a) and 5 day value data sets (b). The eigenvalues for the first mode are shown by a bold line, and those of higher order modes are shown by thin lines. The first EOF mode is clearly predominant, and forms the mainstay of the analysis discussed in the present paper.

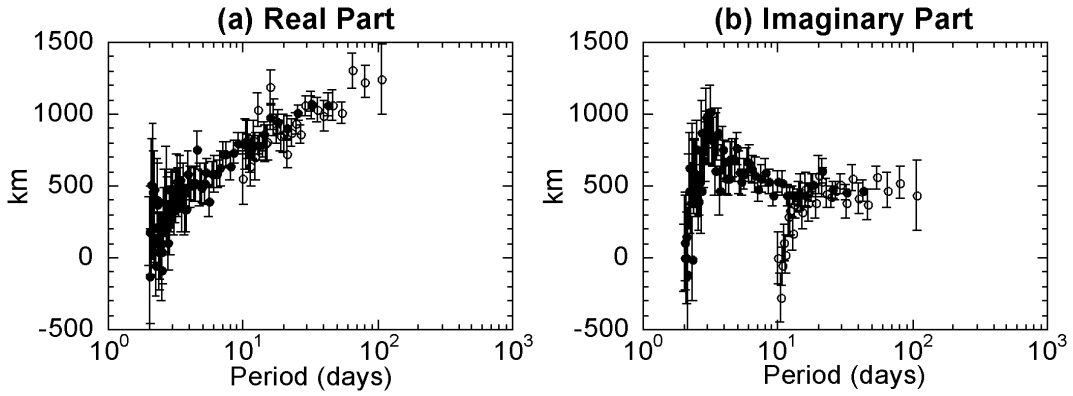

Figure 5. Complex c responses at Kakioka, Japan (26.31°N, 207.25°E in geomagnetic coordinates) which are computed under the P_1^0 source assumption. Left and right panels are the real (a) and imaginary (b) parts, respectively. Estimates derived from the daily data set are marked with solid circles, and those from the 5-day data set with open circles. Delete-one Jackknife estimates of confidence limits are also shown.

Section 4.2) was set to 0.015 and 0.02, respectively, so that a few modes are significant and the noise is not overestimated. It is clear that the first mode (bold line) is dominant at most periods. Eigenvalues of higher modes are less than 10 per cent of the magnitude of the first mode at periods longer than 5 days. This suggests that for most periods the spatial structure of the geomagnetic field variations can be summarized in rather simple form by the first mode exclusively. The magnitude of the higher modes increases near the solar rotation periods of about 27 days and first two harmonics (13 and 9 days), suggesting more complicated spatial structures for those periods. Higher order modes are also seen to peak at periods of about 21 and 17 days in the eigenvalues of the 5-day results.

The uncontaminated Fourier coefficients $\sigma_k \bar{u}_{k1}$ (eq. 12) were used to compute the c response (eq. 2) at Kakioka, Japan under the P_1^0 (i.e. dipolar) source assumption. This provided a check on consistency between the two independent EOF analyses that made use of the daily (solid circles) and 5-day values (open circles) (Fig. 5). The c values were obtained using only the first mode of the two analyses. Inconsistency is seen in the narrow band of 10–13 days period, especially in the imaginary part of c. Confidence limits on c obtained from the 5-day values generally show larger error bars than those obtained from the daily values. This is probably because outliers were not fully corrected in decimation, and the influence of these discordant values is not negligible at the shorter period band end of the spectrum calculated from the 5-day values. Therefore, we use the results of the 5-day values at periods longer than 13 days to augment those obtained at shorter periods from the daily values.

Fig. 6 illustrates the noise variance σ_k vs geomagnetic latitude at 42.7 days period from the daily value analysis. The distributions of the variance are similar to that shown in Fig. 6 for all periods where the first mode is dominant. The data variances for all three components depends on geomagnetic latitude, and the noise level is sharply enhanced at $\sim 55^\circ$ latitude. This suggests that different source field mechanisms may be at play to generate geomagnetic variations at high ($>55^\circ$) and mid- and low ($<55^\circ$) latitudes.

Some observatories show significantly larger variances than others, even in a narrow band of latitudes. These large variances usually correspond to poor data quality, e.g. large data gaps or spurious values that have persisted even after robust downweighting.

Fig. 7 shows the power spectra of the original data and of the first 3 modes at the same period as in Fig. 6. The original data and the corresponding three field components from the first three EOF modes are plotted against geomagnetic latitude. This shows clearly that the first mode (bold solid line) has strongly zonal form because the power spectrum of B_y is small in comparison to that for B_x and B_z, and is associated with the mid- and low latitude variations of B_x and B_z. The higher modes are not necessarily zonal, and have greatest significant at high latitudes. This profile is essentially the same over periods including the solar rotation (27 d) variation and its harmonics. Fig.7 also suggests that B_x and B_z are globally correlated

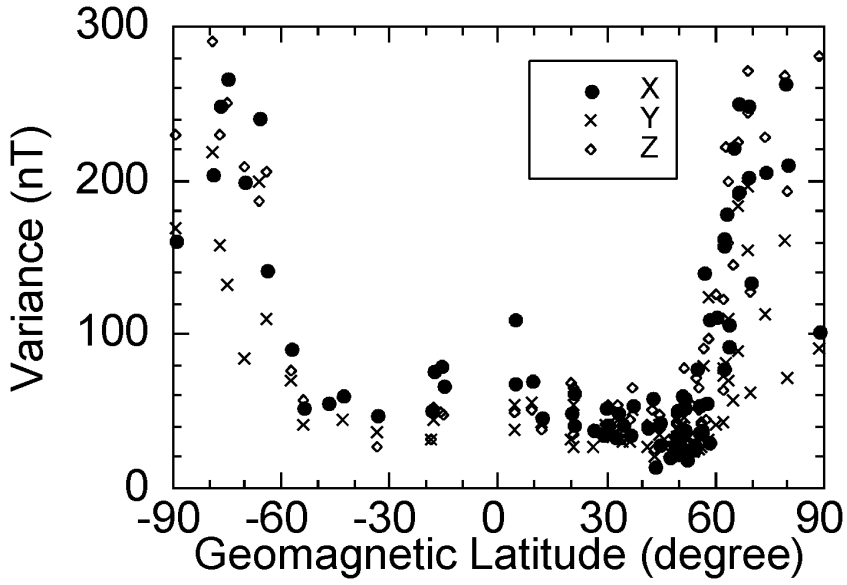

Figure 6. Estimates of the noise variance for the daily data set, at a period of 42.7 days. The variances of B_x, B_y, and B_z components of the geomagnetic field are plotted with solid circles, crosses and open diamonds, respectively.

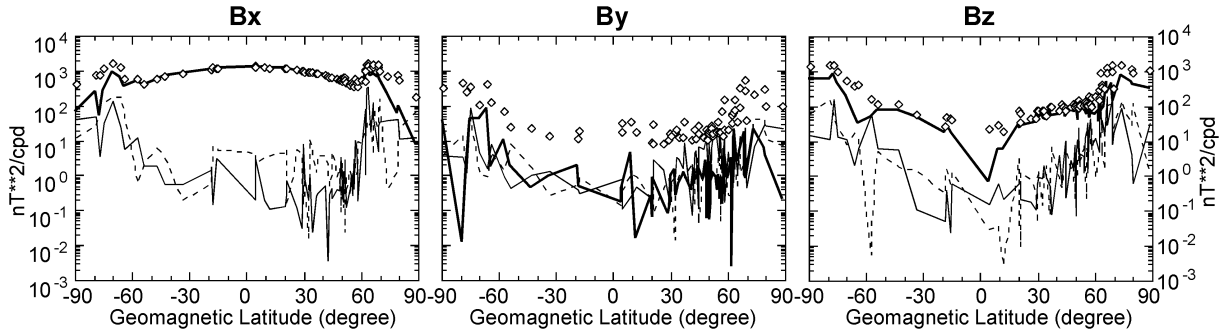

Figure 7. Power spectra of the original geomagnetic field for the daily data set (open diamonds) and first three EOF modes (first mode: thick line, second mode: thin line, third mode: broken line) at a period of 42.7 days, as a function of the geomagnetic latitude. The B_x, B_y, and B_z components are shown from left to right.

and B_y is more localised because the power spectra of the original time-series and that of the EOF modes essentially agree with each other only for B_x and B_z.

The temporal and spatial variance of the fields are dominated by the first EOF mode, explaining approximately 90 per cent of the variance. We have therefore chosen to concentrate on the interpretation and analysis of the first mode for the remainder of the present work. It is seen below that the first mode appears linked to well established magnetospheric and ionospheric source current systems. The interpretation of the higher order modes will be the subject of subsequent analysis.

5.2 First EOF mode

Fig. 8 shows the first mode eigenvector $\sigma_k \bar{u}_{k1}$, $k = 1, \ldots, K$ for 42.7 d period in the form of the three field components. For the B_x and B_z components, a P_1^0 spatial structure is dominant at mid- and low latitudes, and a strong local variation is superimposed on this at high latitudes. The B_y component is of smaller magnitude for mode 1, compared with B_x and B_z, and does not show any systematic latitudinal dependency.

Fig. 9 shows a comparison between the first modes at 42.7, 25.6, 18.3, 12.8 and 7.1 days. The first modes of the B_x and B_z components are normalized such that these field components fit the P_1^0 source functions $\sin(\theta)$ and $\cos(\theta)$, respectively, at the latitude of Kakioka (geomagnetic latitude $\Theta = 90 - \theta = 26.31^\circ$). Kakioka is chosen because it is a mid-latitude site that gives stable EOF and response function estimates at all periods. The spatial structure of the first mode is essentially invariant with period, except at 25.6 and 12.8 days where estimates at very high latitudes become much larger.

Discrepancies between the first mode and the P_1^0 model (i.e. unit sine and cosine functions) become evident in the B_z component at surprisingly low latitudes. Recall that the P_1^0 source terms arise from the relaxation phase of D_{st} variations. This results in modulations of the magnetospheric equatorial ring current system. We can not explain these discrepancies by an equatorially centred source function containing higher degree zonal spherical harmonic terms. An equatorial ring current would contain purely zonal spherical harmonic terms, with the relative magnitude of higher order zonal coefficients dependant upon the radial distance of the ring current from the Earth's surface (e.g. Chapman & Bartels 1940; Eckhardt *et al.* 1963; Banks 1969). We believe these discrepancies arise from the influence of one or more additional external source fields, centred at higher latitudes, and whose influence extends down to $\sim 40^\circ$ for the B_z component and $\sim 50^\circ$ for the B_x component. Figs 8 and

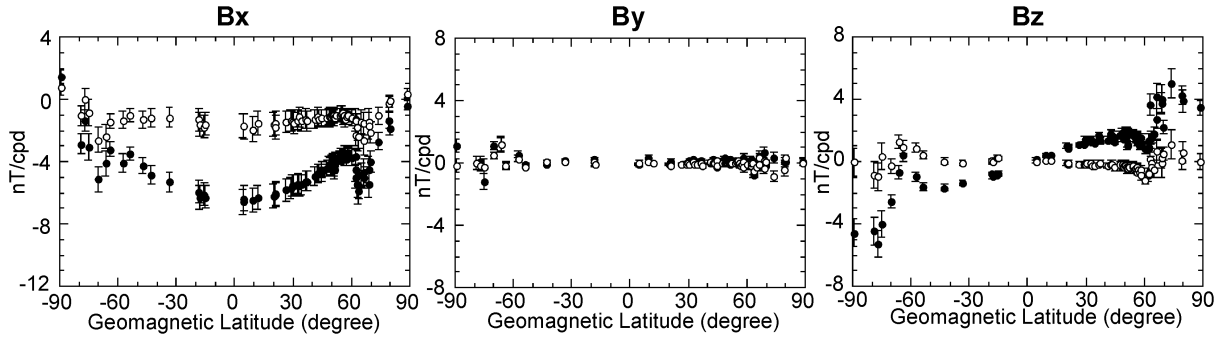

Figure 8. First EOF mode for the daily data set at a period of 42.7 days, decomposed into the three vector components B_x, B_y, and B_z. The real (solid circle) and imaginary (open circle) parts of the field are shown.

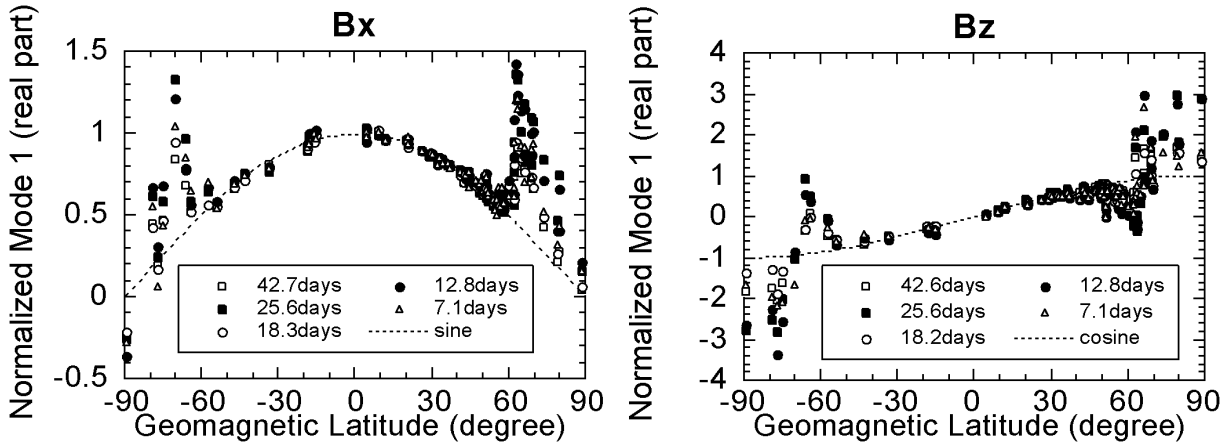

Figure 9. Comparison of first modes at periods of 42.7, 25.6, 18.3, 12.8 and 7.1 days for the daily data set in the B_x (left) and B_z (right) components. The fields are normalized so that they are the best fit to a unit sine (X component) and cosine (Z component) function at the geomagnetic colatitude of Kakioka (26.31°N). The real part is shown here.

9 indicate that over a long-term average, the high latitude current sources and the equatorial current system are correlated with each other.

The influence of higher latitude source currents on B_z and B_x suggests that approximating the geomagnetic field variations by a P_1^0 source will bias estimates of c responses even at mid-latitudes (∼40–50°). Fig. 10 clearly shows that the real parts of c obtained by using the first EOF mode have latitudinal dependencies. We investigate in Section 6 below a method of accommodating high latitude current sources so that the bias in the response functions may be corrected.

6 MODELLING OF THE AURORA RING CURRENT

The first EOF mode of the B_x and B_z geomagnetic field components was seen to contain contributions from two sources with distinct geographical characteristics. A P_1^0 variation predominates at mid to low latitudes, and a more localised variation is predominant at higher latitudes. The localized variation is of zonal form (i.e. independent of longitude) and is centred at about 67°. Not coincidentally, this latitude is the average centre of the statistical auroral oval (Fel'dshteyn 1963; Akasofu 1964). The ionospheric current system which is related to magnetic storms and auroras forms a partial ring at the auroral oval, and another partial ring is simultaneously formed at the conjugate point of the magnetic line in the other hemisphere (e.g. Svalgaard 1975). Our results imply that (1) the first EOF mode of the geomagnetic field variations at periods longer than 5 days is to good approximation generated by two kinds of ring currents in the same direction; an equatorial ring current in the magnetosphere and two conjugate auroral ring currents in the ionosphere, and (2) an average auroral ring current has stationary effects in the geomagnetic field variations at surprisingly long periods.

To verify this assumption, we modelled the magnetic field due to a ring current (cf. Jackson 1975) above a perfectly insulating spherical earth. In these calculations we consider only the source field, and ignore the small induced fields that would arise within the interior of a conducting earth. We consider a loop of current I in the horizontal plane (Fig. 11). The loop is centred on the vertical axis, the distance to the loop from the origin is a, and the colatitude of the loop is θ_c, giving the radius of the loop as $a \sin\theta_c$. Because of symmetry, the magnetic vector potential due to the loop current has only a ϕ-component,

$$A_\phi(r,\theta) = \int_0^{2\pi} \frac{\mu_0}{4\pi} \frac{Ia \sin\theta_c \cos\phi'}{|\mathbf{x}-\mathbf{x}'|}\, d\phi' = \frac{Ia\mu_0 \sin\theta_c}{4\pi} \times \int_0^{2\pi} \frac{\cos\phi'}{\sqrt{r^2+a^2-2ar(\cos\theta\cos\theta_c+\sin\theta\sin\theta_c\cos\phi')}}\, d\phi' = \frac{Ia\mu_0 \sin\theta_c}{\pi\sqrt{r^2+a^2-2ar\cos(\theta+\theta_c)}} \frac{(2-k^2)K(k)-2E(k)}{k^2} \tag{15}$$

where $K(k)$ and $E(k)$ are the complete elliptical integrals of the first and second kinds, respectively and k is

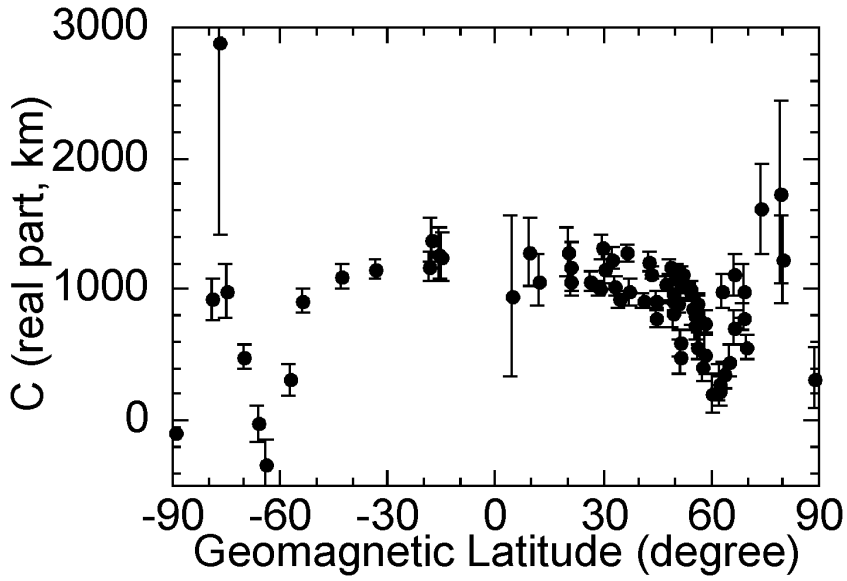

Figure 10. The real part of the complex c responses which are estimated from the first EOF mode at 42.7 days period from the daily data set.

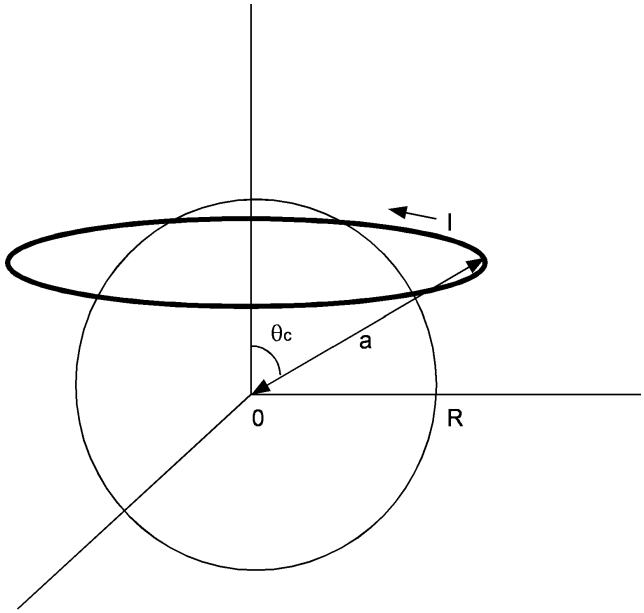

Figure 11. Schematic of a ring current I at colatitude of θ_c and distance from the origin a, and a spherical earth of radius R.

$$k^2 = \frac{4ar\sin\theta\sin\theta_c}{r^2 + a^2 - 2ar\cos(\theta + \theta_c)}. \tag{16}$$

The r and θ components of the geomagnetic field are derived from the potential,

$$B_r = \frac{1}{r\sin\theta}\frac{\partial}{\partial\theta}(\sin\theta A_\phi) = \frac{\mu_0 I}{4\pi r^2\sin\theta\sqrt{r^2 + a^2 - 2ar\cos(\theta + \theta_c)}} \times\left[ar\sin(\theta + \theta_c)f(k) + \frac{(r^2 + a^2)\cos\theta - 2ar\cos\theta_c}{2\sin\theta}g(k)\right], \tag{17}$$

$$B_\theta = \frac{1}{r}\frac{\partial}{\partial r}(rA_\phi) = \frac{-\mu_0 I}{4\pi r\sin\theta\sqrt{r^2 + a^2 - 2ar\cos(\theta + \theta_c)}} \times\left[\{r - a\cos(\theta + \theta_c)\}f(k) + \frac{a^2 - r^2}{2r}g(k)\right],$$

where

$$f(k) \equiv (2 - k^2)K(k) - 2E(k),$$
$$g(k) \equiv -2E(k) - k^2K(k) + (2 - k^2)\Pi(-k^2, k), \tag{18}$$

and Π is the complete elliptical integral of the third kind.

We computed two sets of B_r and B_θ vs. θ at the surface of such a perfectly insulating earth (Fig. 12). Note that $(-B_\theta)$ is the northward component B_x and $(-B_r)$ is the downward positive vertical component B_z. The calculations for Case 1 are for a model of an equatorial ring current centred on the equator ($\theta_c = 90^\circ$). Case 2 is for an auroral ring current whose centre is offset a distance along the rotational axis from the plane of the equator ($\theta_c = 23^\circ$). The distance to the current loop a is parameterized by h, the height of the current loop from the surface of the earth, $a = R + h$ where $R = 6371$ km. The height of the loop in our calculations ranges from 1 to $9R$ (i.e. $a = 2$ to 10 Earth radii) for Case 1 and from 100 to 500 km for Case 2. We set $\mu_0 I/4\pi = 1$ for simplicity. For purposes of comparison, the fields for Case 1 were normalized in the same manner as in Fig. 9.

For Case 1, both B_r and B_θ approach the values of the first order zonal P_1^0 field as h is increased. The P_1^0 spherical harmonic term is a good approximation to the fields for Case 1 when $h \geq 4R$. This is consistent with the conclusion of Chapman & Bartels (1940), Eckhardt *et al.* (1963), and Banks (1969) as used subsequently by many others, that the magnetospheric equatorial ring current may be approximated at mid-latitudes by a first order zonal harmonic. Given a single ring current source located $h \geq 4R$ from the Earth's surface, c values may be calculated on the basis that the B_r and B_θ components of the source field have $\cos(\theta)$ and $\sin(\theta)$ dependence, respectively.

For Case 2, the statistical auroral oval ring current system reproduces the basic features of the localized variation at high latitudes

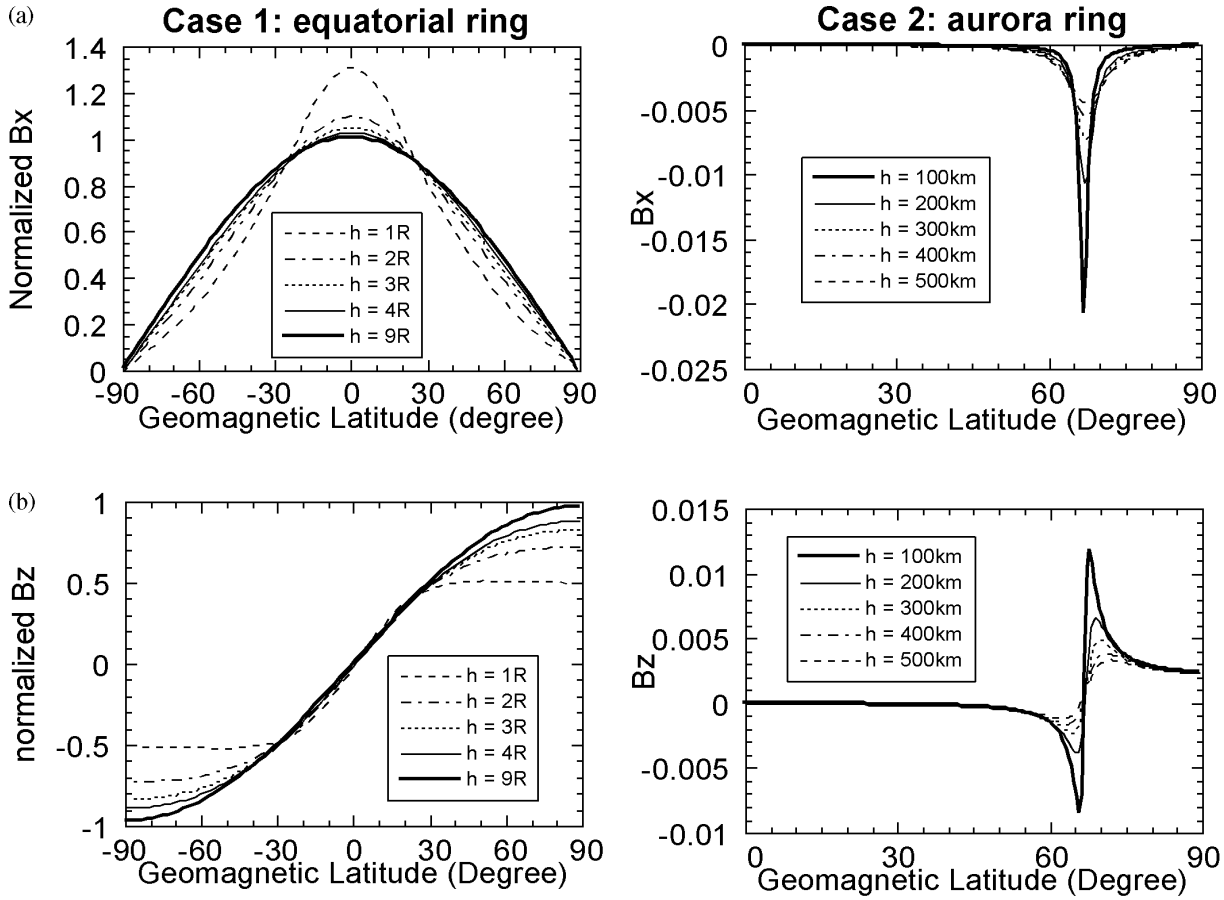

Figure 12. The B_x (a) and B_z (b) components of the geomagnetic field generated by ring currents at latitudes of 0° (left) and 67° (right). The currents are placed at heights varying from 1 to 9 Earth radii (R) for the equatorial ring current case, and from 100 km to 500 km for the auroral current case. The fields of the equatorial ring currents are normalized in the same manner as Fig. 9.

that were seen in Fig. 8. The large variations around $\theta_c = 23^\circ$ are explained qualitatively, as are the tails at mid latitudes. The influence of the auroral oval currents on B_r is observed to reach lower latitudes than for B_θ, whatever height we choose to set h. Since spatial gradients of the field vary strongly with height h at latitudes $>60^\circ$, high accuracy in estimating the EOFs and reproduced fields is necessary if we are to use this to fix the height of the auroral oval current systems with an accuracy of better than ± 100 km.

The modelling of the two ring currents strongly supports the assumption that the source fields have contributions from a magnetospheric equatorial ring current and from the statistical auroral currents. Therefore, we now examine the best composite model of an equatorial and two conjugate auroral ring currents to explain the first mode of the EOF. In principle, the conductivity distribution of the Earth should be known for this purpose. However, it is empirically known that the anomalous field induced by heterogeneities is much smaller than the homogeneous part of the induced field, in other words, the source structure is dominant even in the total field observed at the surface of a laterally heterogeneous conducting earth. Such a result was seen previously in Section 2, e.g. Fig. 1. As a result, given that both source current systems have no B_ϕ component, we can look for a composite source model in which there is no B_ϕ component and in which B_r and B_x are decoupled. We solve for a composite source model that fits the first mode best in a least-squares sense.

The composite model to fit the first mode is

$$B_x(\omega,\theta) = A(\omega)B^e_\theta(h,\theta) + B(\omega)B^a_\theta(H,\theta),$$
$$B_z(\omega,\theta) = C(\omega)B^e_r(h,\theta) + D(\omega)B^a_r(H,\theta), \tag{19}$$

where h and H are the heights of the equatorial and auroral ring currents, respectively, and B^e and B^a represent the geomagnetic fields of equatorial and auroral ring current origin. The parameters to be obtained by statistically robust least-squares fitting are h, H, A, B, C and D.The strong latitudinal dependence of the signal strength and of the uncorrelated noise makes it preferable to fit the B^e and B^a sources to the data separately.

A comparison between the first mode $\sigma_k \bar{u}_{k1}$ at 42.7 days and the equatorial ring current models is shown in Fig. 13. Coefficients A and C were estimated by using data from latitudes $-50^\circ < \Theta < 50^\circ$ for B_x and $-40^\circ < \Theta < 40^\circ$ for B_z. This was done to avoid the influence of the auroral ring current. Models with $h = 4R$ to $h = 9R$ fit better than the others, suggesting that the current is located at relatively great distances. Since differences between models with $h > 4R$ are subtle, as shown in Fig. 12, the height of the equatorial ring current can be fixed arbitrarily somewhere higher than $4R$. We choose to subtract the field due to the equatorial current at $h = 9R$ from the first EOF mode at all latitudes.

Data from latitudes of $-70^\circ < \Theta < -50^\circ$ and $50^\circ < \Theta < 70^\circ$ for B_x, and at $-70^\circ < \Theta < -40^\circ$ and $40^\circ < \Theta < 70^\circ$ for B_z were used to

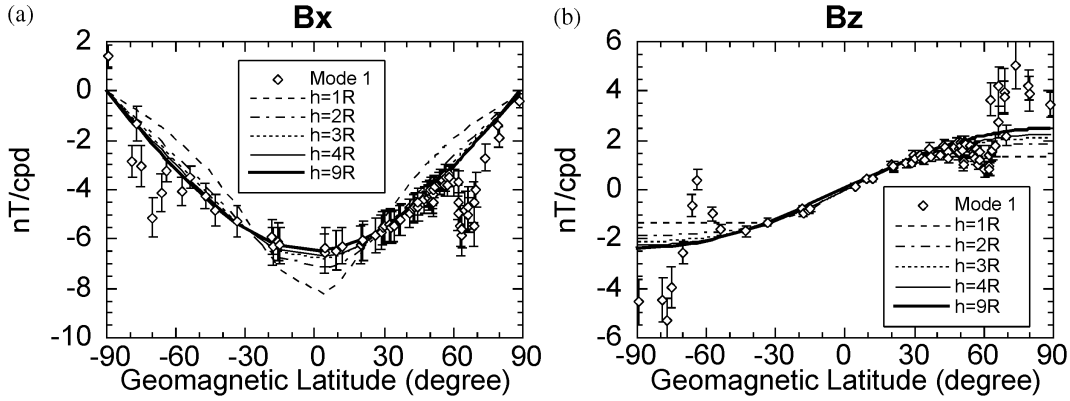

Figure 13. Least squares fit of the equatorial ring current models (5 lines) to the first mode (open diamonds) in the B_x (left) and B_z (right) components at 42.7 days period, for the daily data set. The heights of the ring currents are the same as Fig. 12.

fit the conjugate auroral ring currents in the same direction. Data at very high latitudes were not used because of large confidence limits and low data quality, as implied in Fig. 6.

The substantial scatter in the B_z component data leads us to adopt a hard rejection robust procedure for fitting this component. Here, data found to be discordant by the robust statistical procedures were eliminated entirely from the analysis. A soft rejection robust procedure was used to fit the B_x component data. In this case, the influence of data found to be discordant was downweighted. The discordant data were identified through calculating the residuals,

$$\begin{aligned} r_x(\omega,\theta,\phi) &= \hat{B}^1_\theta(\omega,\theta,\phi) - B^a_\theta(\omega,\theta,\phi) \\ r_z(\omega,\theta,\phi) &= \hat{B}^1_r(\omega,\theta,\phi) - B^a_r(\omega,\theta,\phi) \end{aligned} \tag{20}$$

where the hat and superscript 1 refers to the magnetic field component calculated from EOF mode 1 with the equatorial current effect removed. For the hard rejection procedure, data were rejected if their individual residuals $r_z(\omega,\theta,\phi)$ exceeded four times the median absolute deviation of all the residuals over the Earth's surface. In the worst case, 20 per cent of the data were rejected.

Fig. 14 shows the results of fitting the auroral oval current system fields to the observed fields from EOF mode 1 for a period of 42.7 days. Since data coverage from the southern hemisphere is sparse and EOF estimates there are demonstrably less stable than those from the northern hemisphere, Fig. 14 shows only the results from the northern hemisphere. The source field dependence on H becomes clear at $\theta \geq 60^\circ$, and models with $H = 300$–500 km fit the data better than those with $H = 100$–200 km. Data scatter makes it difficult to choose precisely which is the best model.

Direct observation of the auroral current systems by radiosonde and radar-borne sensors indicates that the basal layer of the auroral current sheets extends down to 90 km from the Earth's surface, while the upper boundary extends to 200 km (Brekke *et al.* 1974; Brekke & Moen 1993). Part of the discrepancy may be attributed to the use of an idealised representation of the auroral current systems as infinitesimally thin line currents rather than sheets of finite thickness, and part may be due to ignoring secondary induction effects in the auroral currents as described in the introduction to the present section.

The various models explain the latitudinal dependency of B_x and B_z equally well for $\Theta < 60^\circ$. Fig. 15 shows c responses of eq. (13) at 42.7 days which are calculated by using the first mode, with the contribution of B^a removed from B_x and B_z. The latitudinal dependence of the c response is significantly reduced in comparison with c values calculated by assuming the source is exclusively of P_1^0 form. These are shown as grey circles in Fig. 15. In contrast, the d response, which arises from non-zero B_ϕ components, is more weakly affected by accounting for the source effects of the auroral current system. For subsequent calculations, we set $H \cong 300$ km and limit the use of B^a at mid- and low latitudes.

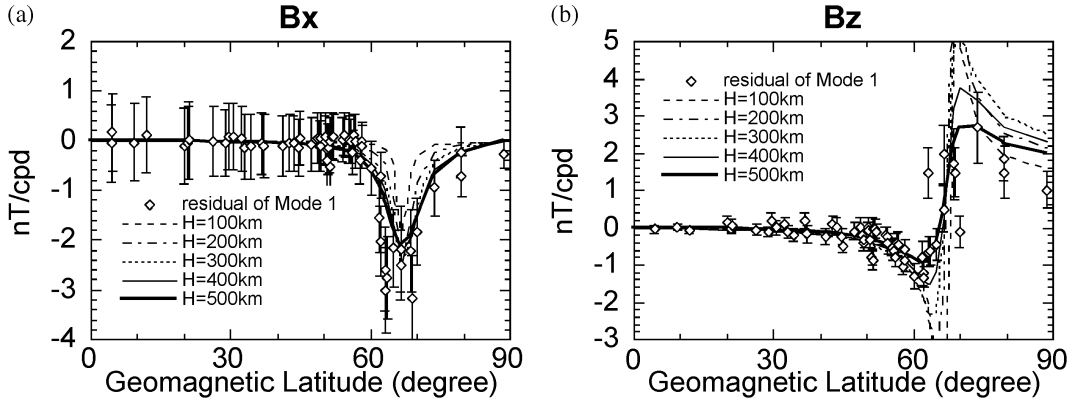

Figure 14. Least squares fit of the auroral ring current models (5 lines) to the residual of the first mode (open diamonds) in the B_x (a) and B_z (b) components at 42.7 days period, for the daily data set. The best fitting model of the equatorial ring current at a height of 9 R is subtracted from the first mode. The heights of the ring currents are the same as Fig. 12.

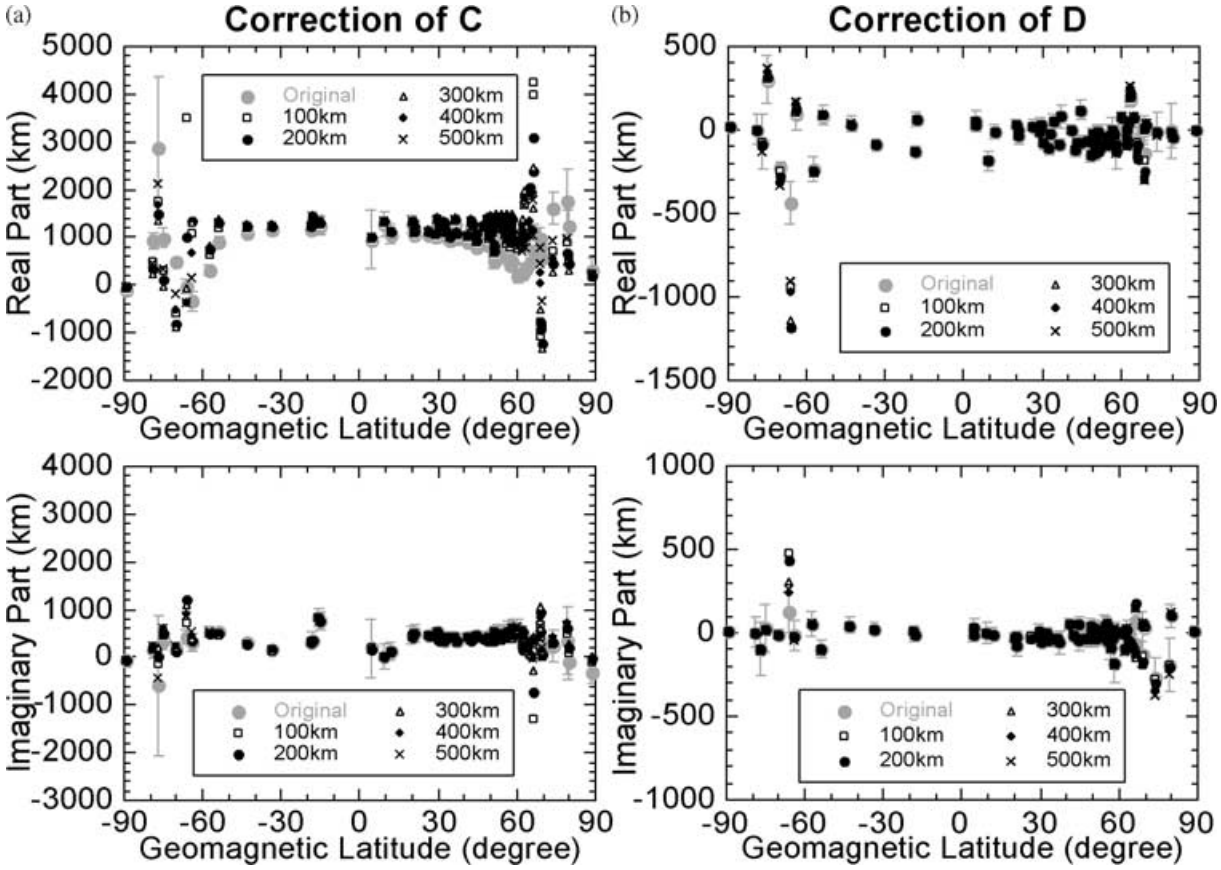

Figure 15. *c* (a) and *d* (b) responses at period of 42.7 days for the daily data set, with correction of the auroral ring current effects. The 5 models shown in Fig. 14 are subtracted from the B_x and B_z components of the first mode in turn, and the *c* and *d* responses are recomputed. The original responses (grey circles) are also shown for reference.

7 *c* AND *d* RESPONSES

Fig. 16 shows the geographical distribution of the *c* response with the auroral ring current effects corrected. The auroral ring current model with $H = 300$ km is chosen to correct the first mode, and the *c* response is computed with the B_x and B_z components corrected over the latitude range of $-60^\circ < \Theta < 60^\circ$. The response increases smoothly with period for most of the observatories. Observatories where the responses show relatively extreme values (e.g. M'Bour, Alibag and Guam) have large confidence limits or large noise variances, as seen in Fig. 6. Therefore, we regard the responses for those station locations as only poorly constrained.

The exceptions to this are the two observatories at the southern tip of Africa (Hermanus and Tsumeb). They consistently show smaller values in the imaginary part of *c*, and estimates are statistically reliable. This is especially true at Hermanus. This is in contrast to our previous attempts to estimate *c* values for Hermanus by assuming a purely P_1^0 source field configuration. Those efforts in the early 1980*s*, resulted in non-physical values, and were not included in published catalogue of *c* responses (e.g. Schultz & Larsen 1987).

Within the global collection of *c* responses we have calculated, if extreme values are removed the total variation in magnitude of the real part of the *c* response for a given period is about 1000 km. The relatively dense magnetic observatory networks in Europe and the Far East make investigation of regional-scale conductivity structures possible. The geographical variations in *c* for these two regions are smooth and do not reflect the variations in geomagnetic latitude shown previously in Fig. 10. This suggests that the primary effect of the auroral ring current has been corrected successfully. Additional future refinements on these corrections may be possible if we account for internal EM induction when fitting the auroral source term.

Fig. 17 compares the present uncorrected and corrected *c* responses to the collection of responses published by Schultz & Larsen (1987). We have selected data from four observatories that provide *c* responses of high quality. The *c* responses of the daily data set from 5 to 42.7 days, and of the 5-day data set from 13 to 106.6 days are shown with the associated Jackknife error estimates. The effects of applying the auroral current corrections are almost within the confidence limits of the *c* estimates at the latitudes of $\sim 20^\circ$, $\sim 30^\circ$ and $\sim 40^\circ$ (Kanoya, Memanbetsu, and Irkutsk). However, the corrected values are far beyond the confidence limits on *c* for 50° latitude (Witteveen), regardless of the value of *H*.

Schultz & Larsen (1987) published a collection of *c* responses which is generally in good agreement with the present collection of uncorrected (i.e. assumed P_1^0 source) *c* responses. This is reassuring, given the great differences between geomagnetic time-series data catalogues and methods of analysis available to both studies.

Fig. 18 shows comparison with Olsen's (1998) *c* responses at Fuerstenfeldbruck ($\Theta = 48.55^\circ$). As for Witteveen in Fig. 17, differences between the uncorrected and corrected *c* responses are significant. Olsen's (1998) results show good agreement with the uncorrected *c* for the real part and a different trend to the present *c* for the imaginary part. The present and Schultz & Larsen's (1987)

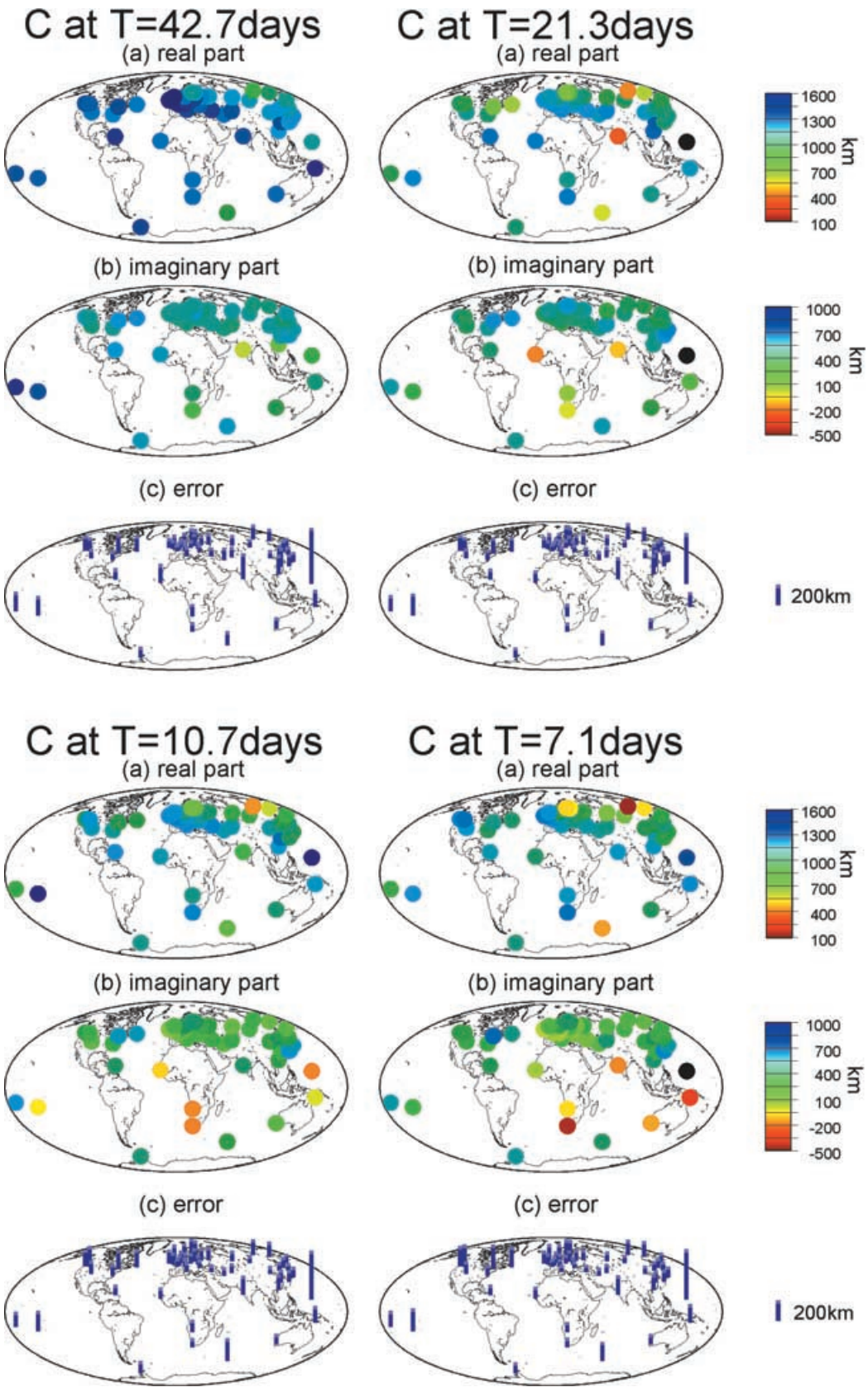

Figure 16. Geographical distribution of the *c* response at periods of 42.7, 21.3, 10.7 and 7.1 days for the daily data set. For each period, the real part (top), imaginary part (middle) and delete-one Jackknife confidence limits (bottom) are shown. The *c* responses are computed from the *x* and *z* components of the first mode, with the auroral ringcurrent effects corrected. The height of the aurora ring current is taken to be 300 km.

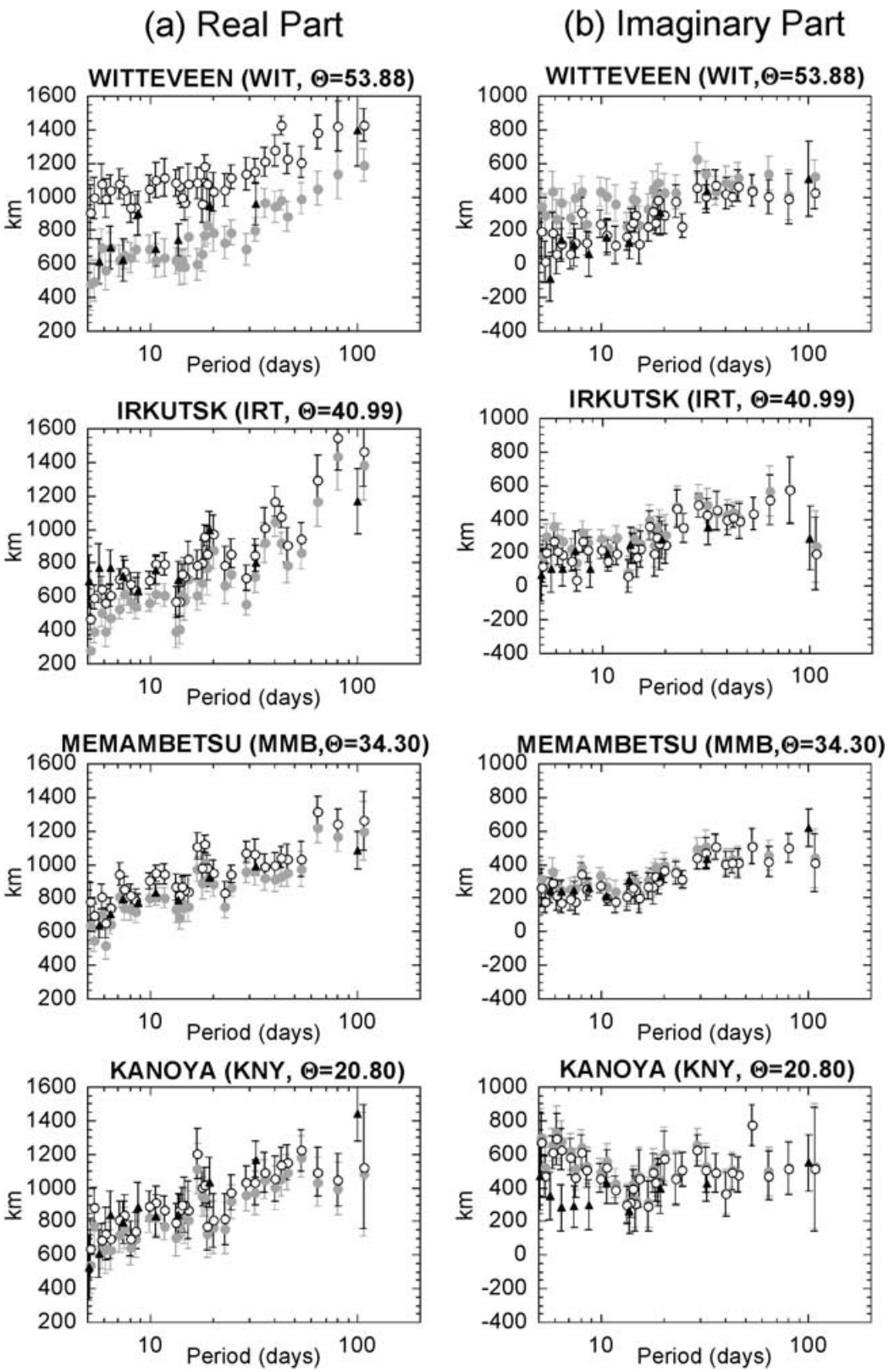

Figure 17. Comparison of the *c* responses at Witteveen, Irkutsk, Memambetsu, and Kanoya from the top to bottom. The estimates from the first mode with (grey circles) and without (open circles) the auroral ring current effects, and estimates by Schultz & Larsen (1987) (solid triangles) are compared in the real (a) and imaginary (b) parts. The results of the daily data set at periods from 5 to 42.7 days and of the 5-day data set at periods from 13 to 106.6 days are shown with the Jackknife error (common between grey and open circles). The height of the auroral ring current is 300 km.

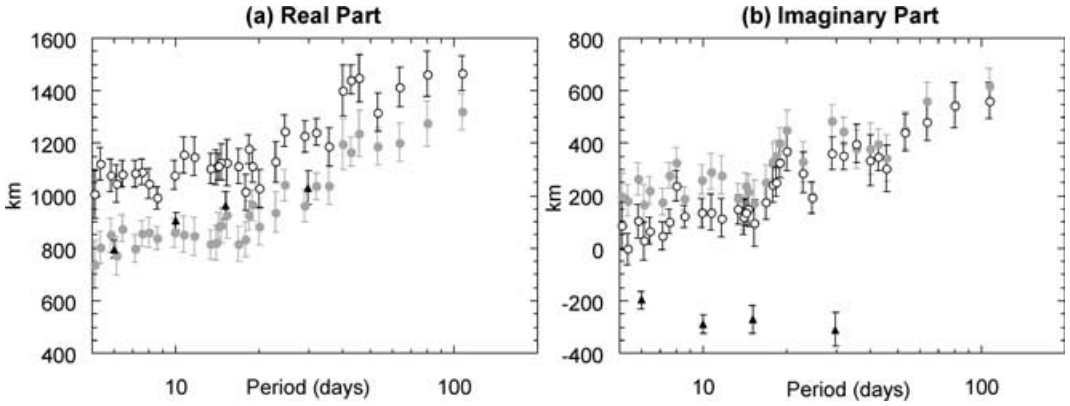

Figure 18. Comparison of the *c* responses at Fuerstenfeldbruck. The estimates from the first mode with (grey circles) and without (open circles) the auroral ring current effects, and estimates by Olsen (1998) (solid triangles) are compared in the real (a) and imaginary (b) parts in the same manner as Fig. 17.

collections in Europe are generally similar to each other except for the auroral effects, while Olsen's (1998) collection in the region generally show discrepancies in the imaginary part. This may be a qualitative difference between two groups of the *c* response collections.

The sensitivity of the uncorrected *c* responses to the effects of the auroral oval at higher latitudes does suggest that the earlier published collection of *c* responses may be biased by auroral current system effects at these latitudes. This will not effect the bulk of the published responses, as these are associated with mid and lower-latitude sites, but it does offer an insight into the difficulty previous studies faced in obtaining physically plausible *c* values at geomagnetic latitudes above approximately 50°. This bias is clearly detected here for the first time through the application of statistically robust EOF analysis and the approximate quadrupling of geographical data coverage in the present catalogue of magnetic observatory time-series records compared with that previous study.

The present estimates of *c* at low latitudes and some mid latitude observatories are not reliable, as shown in Figs 10 and 16, while Schultz & Larsen (1987) successfully computed local *c* responses there. There may be two reasons for this. There may be some spurious values remaining in the B_z component that act to contaminate calculations of EOF mode 1. This arises because B_z is of smaller amplitude at low latitude, and spurious values of a given magnitude consequently have a greater impact on the analysis. This situation can probably be improved in future by modifying the influence functions used in the robust EOF analysis to accommodate smooth functional dependence on latitude.

Also, the data from these observatories contain large data gaps in the time period used in this study. Some improvement in the reliability of response estimates can be expected if another time period is used. We have carried out a number of preliminary computations in order to identify more optimal time periods in this respect. The low order EOF modes for different time periods show good agreement if the data sets contain a similar number of observatories. Replacement of bad estimates, or addition of new estimates from another data set will be a practical approach to build a better set of *c* responses.

Fig. 19 shows the geographical distribution of the *d* response of eq. (14) obtained by using the first mode, with the auroral ring current effects in the B_x component corrected. The geographical variability of *d* is much smaller than that of *c*, while the confidence limits are much larger. The B_y component is weaker than the B_x or B_z components, and the *d* response (the scaled ratio of $B_y : B_x$) is likely to be particularly sensitive to spurious values in B_y. The contribution to the first mode can be underestimated if the data are too noisy. We should be careful about the use of the *d* responses at observatories with low quality indicated in Fig. 6. On the other hand, in regions like Europe and the Far East, where the data are dense and stable, non-zero *d* responses vary smoothly with period and geographical position. This is now proving an important additional constraint in efforts to model the underlying heterogeneities in deep mantle electrical conductivity.

8 EQUIVALENT CURRENT SYSTEMS

As another way of displaying the effects of 1D and 3D mantle conductivity structure on the observed fields, we estimated an equivalent sheet of the internal electric current system (Fig. 20). Several approaches may be taken for such a calculation, each representing the 'true' internal current distribution in successively better approximation. First, one may calculate the internal **B** fields, and rotate these by 90 degrees. This would be equivalent to the **E** fields in a vacuum or within an infinite homogenous conductive space, from which electric current density **J** may be determined. A finer level of approximation would arise by calculating $\nabla \times \mathbf{B}$, which through Maxwell's equations would be related directly to the electric current density, i.e. $\mathbf{J} = \sigma \nabla \times \mathbf{B}/\mu$. In the thin sheet approximation, vertical gradients in the horizontal **B** field components could be ignored in the calculation of the curl. An even more realistic approximation would arise from calculating the equivalent internal fields due to an *a priori* 1D reference model from which vertical gradients in the horizontal **B** fields could be obtained. Finally, the 'true' current systems could be determined if the true Earth conductivity distribution were known, but of course this is the goal of the inverse problem.

In the present work we have taken the simplest approach, i.e. displaying equivalent current distributions *in vaccuo*. While not entirely satisfactory, it does prove a useful indicator of the presence of conductive and resistive anomalies in the mantle. For purposes of guiding inverse-modelling efforts, it is probably useful to establish a 1D background conductivity model both for calculating equivalent current systems more accurately, and for use as a starting model for 3D inversion.

In order to estimate the equivalent current sheets due only to the presence of 3D anomalous features in the Earth's interior, it is necessary first to remove the induction effects related to an underlying 1D (radial) conductivity structure. The procedure to compute this as follows. The fields expected on the surface of an insulating Earth due to the presence of the equatorial magnetospheric ring and

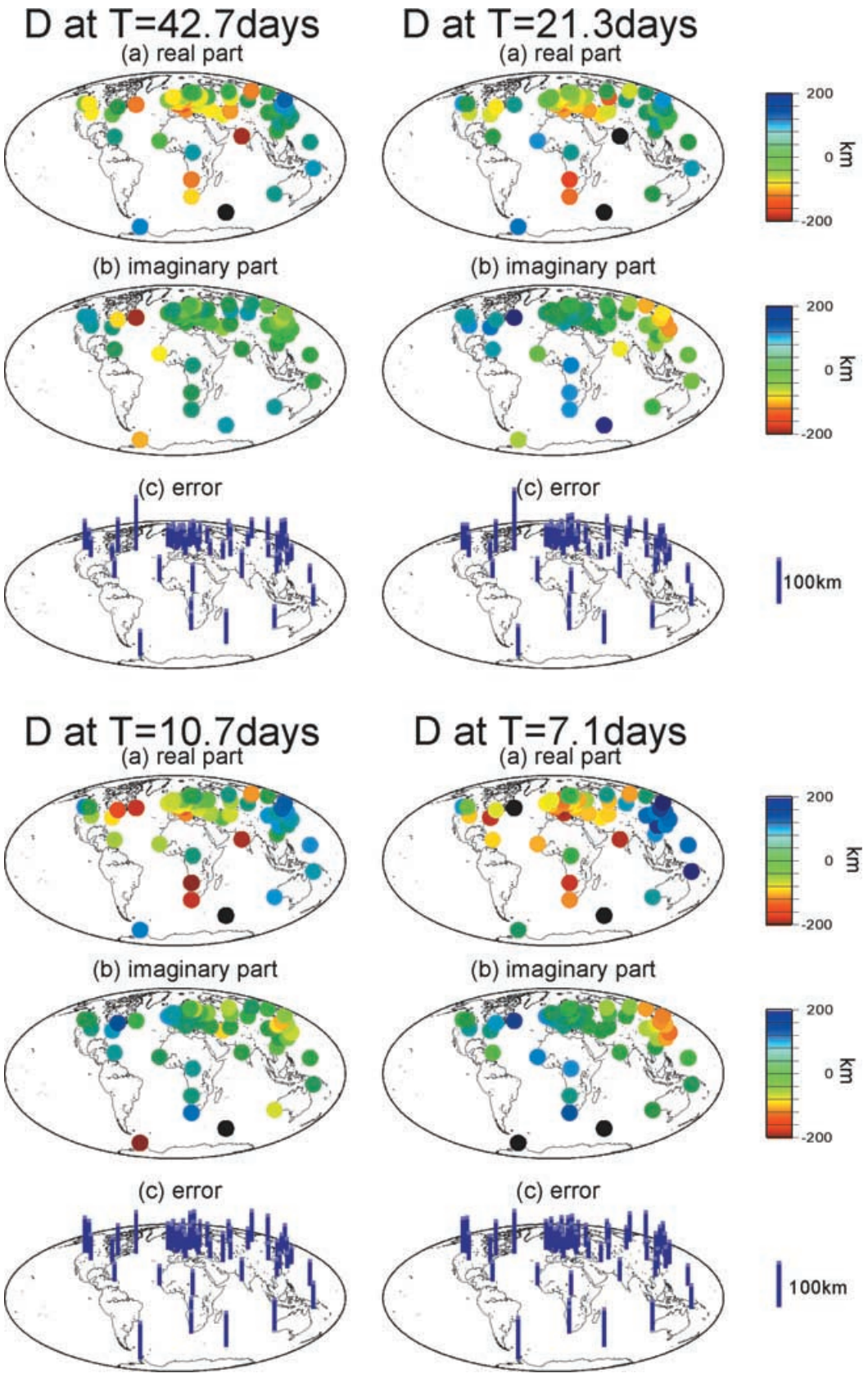

Figure 19. Geographical distribution of the *d* response at periods of 42.7, 21.3, 10.7 and 7.1 days for the daily data set. At each period, the real part (top), imaginary part (middle) and delete-one Jackknife confidence limits (bottom) are shown. The *X* component of the first mode, with the aurora ring current effects corrected, and the *Y* component of the first mode are used to compute the *d* response. The height of the aurora ring current is taken to be 300 km.

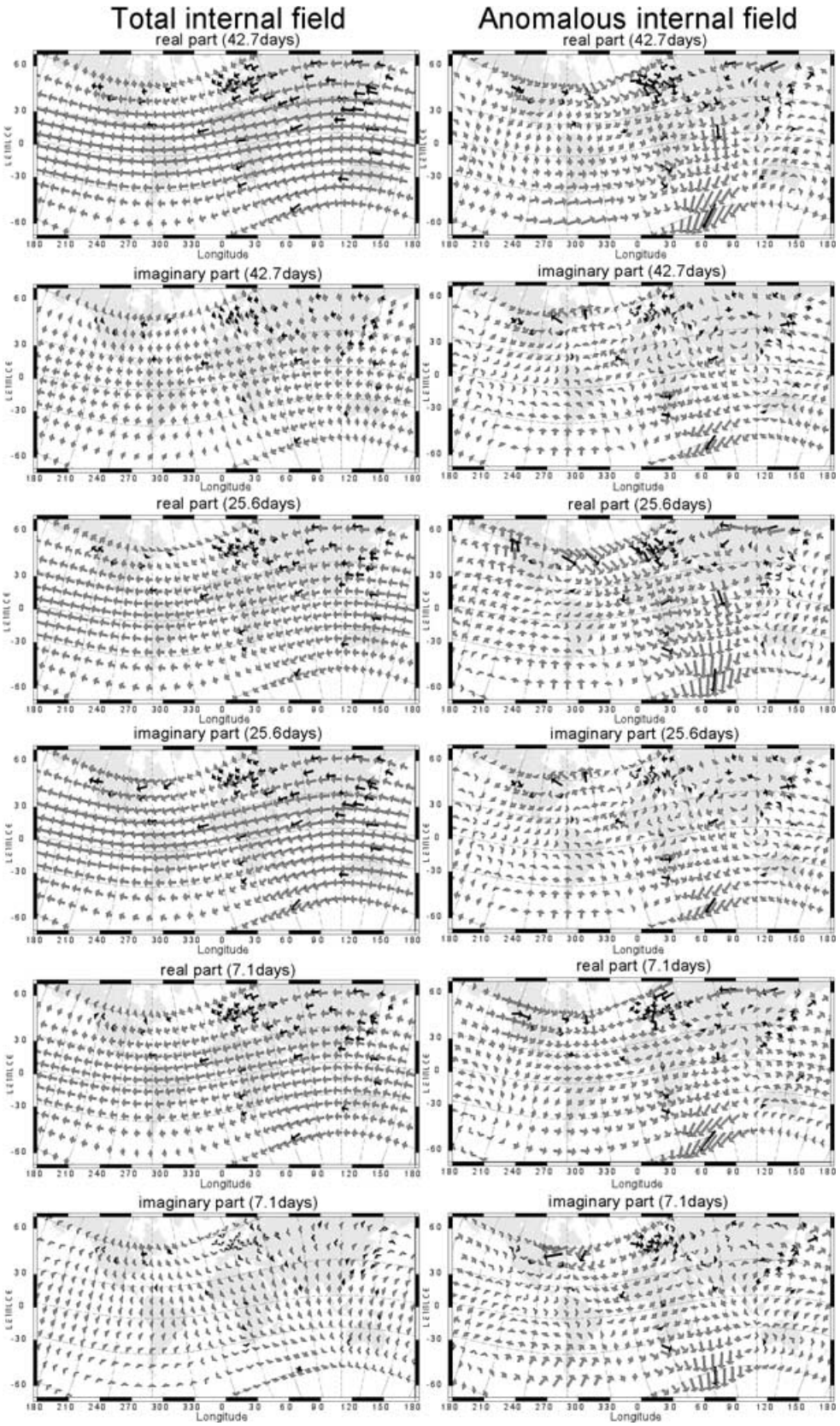

Figure 20. Equivalent current system **J** determined from the internal part of the First EOF mode without the auroral current effect at 42.7, 25.6 and 7.1 days. The geographical coordinates are used for drawing and latitudinal and longitudinal lines on the geomagnetic coordinates are also shown every 30°. The real and imaginary parts of the total and anomalous electric currents were shown at $11^\circ \times 10^\circ$ grid points in the geomagnetic coordinates (grey arrows) and 52 observatories (black arrows). The vectors on a $11^\circ \times 10^\circ$ grid were interpolated with a natural interpolator from the observed ones at 55 and 52 observatories for B_x and B_y components, respectively.

auroral oval current systems were calculated for the first EOF mode. Scaling factors were applied to these theoretical fields such that the observed fields were best fit in a least-squares sense. Such a scenario would represent both the external source fields and the internal induced fields for an Earth with purely 1D (radial) conductivity variation. We regard the residual as the anomalous geomagnetic field which is produced by 3D conductivity variations relative to the 1D background.

Since both the auroral and equatorial current systems are zonal, the B_x and B_z components of the first mode are affected by subtracting the reference field. Considering the large scatter in the first mode at high latitudes, data at $-60^\circ < \Theta < 60^\circ$ were used in the next step. Amplitudes of anomalous B_x and B_y are comparable within this latitude band. The anomalous B_x and B_y at 55 and 52 observatories, respectively, were interpolated onto a regular $11^\circ \times 10^\circ$ grid by using a natural interpolator (Schultz & Pritchard 1999) to obtain values for the anomalous horizontal field. This process resulted in a geographical map of the fields due to anomalous (i.e. 3D) conducting regions in the Earth's interior.

In order to obtain equivalent current sheet models for the total internal field, rather than just for the anomalous (i.e. 3D) field, spherical harmonic decomposition was applied to B_x and B_z of equatorial ring current origin to separate the internal and external components. The P_1^0 and P_3^0 terms were included in the spherical harmonic expansion although amplitudes of the P_3^0 term were about 1000 times smaller than those of the P_1^0 term. The total internal component was estimated by adding the internal component of equatorial ring current origin to the anomalous field. Finally, the vector was rotated counter-clockwise by 90° to represent the electric field (*in vaccuo*) rather than the magnetic field.

Fig. 20 shows the real and imaginary parts of the total and anomalous electric fields at 42.7, 25.6 and 7.1 days. The anomalous field was multiplied by a factor 4. The original vectors were shown with black arrows at 52 observatories where both B_x and B_y were available, and the interpolated vectors were shown with grey arrows. Figures were drawn on the geographic coordinates and latitudinal and longitudinal lines on the geomagnetic coordinates were shown at every 30°.

It is obvious that the P_1^0 component is dominant in the total internal field at all periods, however regional and period dependencies are seen in the anomalous field. Europe and southern Africa have relatively large anomalies in both zonal and meridional components at all periods, while the Far East tends to have mainly the meridional component and the anomalous part is likely to be larger at shorter periods. The vectors at 25.6 days have larger imaginary parts than those at periods free from 27 days signal and its harmonics, and notably the direction of the meridional anomaly in the Far East is reversed. This probably means that the first mode at 27 days and its harmonics reflects a slightly different source current system than the simple auroral and equatorial ring currents found to explain the variance of the fields at other periods.

9 CONCLUSIONS

We have compiled a new catalogue of the geoelectromagnetic response of the Earth as a necessary step in gaining new insight about the electrical conductivity of the Earth's mantle. The new catalogue is improved over previous versions with respect to both quantity and quality of data. Geographical coverage of the response is greatly improved by construction of a new database of the geomagnetic hourly means and through application of statistically robust estimation methods. The use of robust Empirical Orthogonal Function analysis enables us to estimate spatially and temporally coherent geomagnetic field variations on a global scale. The EOF results suggest that, in a statistical sense, the geomagnetic field variation can be represented predominantly by one mode at periods from 5 to 106.7 days, for which we find that the primary-source fields consist of two current systems: an equatorial ring current in the magnetosphere, and two conjugate auroral oval ring currents in the ionosphere. The influence of the auroral current system is seen at surprisingly low latitudes, 40° and 50° for B_z and B_x, respectively.

We have made a preliminary correction of the auroral current effects on *c* responses that were calculated under the normal assumption that the source fields have P_1^0 geographical form. The results reveal the existence of non negligible bias on such responses, particularly at higher latitudes. Earlier attempts to model the mantle through analysis of *c* responses that ignored auroral induction effects may have encountered difficulties, including the inability to obtain responses that were consistent simultaneously with a local 1D interpretation and P_1^0 source, specifically at higher latitudes.

A new catalogue of *c* responses uncontaminated by auroral current effects shows clear geographical variations implying large scale heterogeneities of the mantle. We have also proposed a new response function *d*. The *d* response is much more sensitive to mantle heterogeneities than the *c* response, particularly for zonal source field excitation. The *d* response represents the degree of heterogeneity and the *c* response reflects a regional conductance. The distribution of non-zero values of the *d* response also supports the existence of large scale heterogeneities of the mantle and will add a new constraint to mantle conductivity modelling. This view of a heterogeneous mantle is supported further by the calculation of equivalent currents in the Earth's interior which show the concentration and diversion of induced currents into and around conductive and resistive bodies, respectively.

ACKNOWLEDGMENTS

We thank the WDCs and geomagnetic observatories for providing data for this study. The EPSRC and JSPS supported this work.

REFERENCES

Akasofu, S.-I., 1964. The development of the auroral substorm, *Planet. Space Sci.,* **12,** 273–282.

Anderson, T.W., 1963. Asymtotic theory for principal component analysis, *Annals of Mathematical Statistics,* **34,** 122–148.

Bahr, K., Olsen, N. & Shankland, T.J., 1993. On the combination of the magnetotelluric and the geomagnetic depthsounding methods for resolving an electrical-conductivity increase at 400 km depth, *Geophys. Res. Lett.,* **20,** 2937–2940.

Bai, Q. & Kohlstedt, D.L., 1992. Substantial hydrogen solubility in olivine and implications for water storage in the mantle, *Nature,* **357,** 672–674.

Banks, R., 1969. Geomagnetic variations and the electrical conductivity of the upper mantle, *Geophy. J. R. astr. Soc.,* **17,** 457–487.

Banks, R. & Ainsworth, J.N., 1992. Global induction and the spatial structure of mid-latitude geomagnetic variations, *Geophy. J. Int.,* **110,** 251–266.

Barton, C.E., 1997. International Geomagnetic Reference Field: the seventh generation, *J. Geomag. Geoelectr.,* **49,** 123–148.

Boschi, L. & Dziewonski, A.M., 1999. High- and low-resolution images of the Earth's mantle: Implications of different approaches to tomographic modeling, *J. geophys. Res.,* **104,** 25 567–25 594.

Brekke, A., Doupnik, J.R. & Banks, P.M., 1974. Incoherent scatter measurements of E region conductivities and currents in the auroral zone, *J. geophys. Res.,* **79,** 3773–3790.

Brekke, A. & Moen, J., 1993. Observations of high latitude ionospheric conductances, *J. Atmos. Terres. Phys.,* **55,** 1493–1512.

Chapman, S. & Bartels, J., 1940. Geomagnetism, Oxford University Press, London.

Chave, A.D., Thomson, D.J. & Ander, M.E., 1987. On the robust estimation of power spectra, coherences, and transfer functions, *J. geophys. Res.,* **92,** 633–648.

Chave, A.D. & Thomson, D.J., 1989. Some comments on magnetotelluric response function estimation, *J. geophys. Res.,* **94,** 14 215–14 226.

Davis, R.E., 1976. Predictability of sea surface temperature and sea level pressure anomalies over the North Pacific Ocean, *J. Phys. Oceanography,* **6,** 249–266.

Eckhardt, D., Larner, K. & Madden, T., 1963. Long-period magnetic fluctuations and mantle electrical conductivity estimates, *J. geophys. Res.,* **68,** 6279–6286.

Egbert, G.D., 1997. Robust multiple-station magnetotelluric data processing, *Geophys. J. Int.,* **130,** 475–496.

Egbert, G., Booker, J. & Schultz, A., 1992. Very long period magnetotellurics at Tucson Observatory: Estimation of Impedances, *J. geophys. Res.,* **97,** 15 113–15 128.

Fel'dshteyn, Ya.I., 1963. Some problems concerning the morphology of auroras and magnetic disturbances at high latitudes, *Geomag. Aeron.,* **3,** 183–192.

Fukao, Y., 1992. Seismic tomogram of the Earth's mantle: Geodynamic implications, *Science,* **23,** 625–630.

Gauss, C.F., 1838. Allgemeine Theorie des Erdmagnetismus, in *Resultate aus den Beobachtungen des Magnetischen Vereins im Jahre 1838,* pp. 1–57, eds Gauss, C.F. & Weber, W., Weidmann, Leipzig.

Hamming, R.W., 1977. Digital filters, Prentice-Hall, Inc., Englewood Cliffs.

Hirsh, L.M., Shankland, T.J. & Duba, A.G., 1993. Electrical-conduction and polaron mobility in Fe-bearing olivine, *Geophys. J. Int.,* **114,** 36–44.

Huber, P.J., 1981. Robust Statistics, John Wiley, New York.

Jackson, J.D., 1975. Classical Electrodynamics, John Wiley, New York.

Karato, S., 1990. The role of hydrogen in the electrical conductivity of the upper mantle, *Nature,* **347,** 272–273.

Lahiri, B. & Price, A., 1939. Electromagnetic induction in non-uniform conductors, and the determination of the conductivity of the earth from terrestrial magnetic variations, *Phil. Trans. R. Soc. Lond.,* A., **237,** 509–540.

Lizarralde, D., Chave, A., Hirth, G. & Schultz, A., 1995. Long period magnetotelluric study using Hawaii-to-California submarine cable data: implications for mantle conductivity, *J. geophys. Res.,* **100,** 17 837–17 854.

Lorenz, E.N., 1956. Empirical orthogonal functions and statistical weather prediction, *Report No. 1, Statistical Forecasting Project,* Dept. Meteorology, MIT, p. 49.

Neal, S.L., Mackie, R.L., Larsen, J.C. & Schultz, A., 2000. Variations in the electrical conductivity of the upper mantle beneath North America and the Pacific Ocean, *J. geophys. Res.,* **105,** 8229–8242.

Olsen, N., 1998. The electrical conductivity of the mantle beneath Europe derived from C-response from 3 h to 720 h, *Geophys. J. Int.,* **133,** 298–308.

Olsen, N., 1999. Long-period (30 days-1year) electromagnetic sounding and the electrical conductivity of the lower mantle beneath, *Geophys. J. Int.,* **138,** 179–187.

Preisendorfer, R.W. & Barnett, T.P., 1977. Significance tests for empirical orthogonal functions, *Proceedings of the Fifth Conference on Probability and Statistics,* Las Vegas, American Meteorological Society, 169–172.

Schmucker, U., 1970. Anomalies of geomagnetic variations in the Southwestern United States, *Bull. Scripps Inst. Oceanogr.,* **13,** 1–165.

Schmucker, U., 1999a. A Spherical harmonic analysis of solar daily variations in the years 1964–1965: response estimates and source fields for global induction—I. Methods, *Geophys. J. Int.,* **136,** 439–454.

Schmucker, U., 1999b. A Spherical harmonic analysis of solar daily variations in the years 1964–1965: response estimates and source fields for global induction—II. Results, *Geophys. J. Int.,* **136,** 455–476.

Schultz, A. & Larsen, J.C., 1987. On the electrical conductivity of the mid-mantle—I. Calculation of equivalent scalar magnetotelluric response functions, *Geophys. J. R. astr. Soc.,* **88,** 733–761.

Schultz, A. & Larsen, J.C., 1990. On the electrical conductivity of the mid-mantle: II. Delineation of heterogeneity by application of extremal inverse solutions, *Geophys. J. Int.,* **101,** 565–580.

Schultz, A., Kurtz, R.D., Chave, A.D. & Jones, A.G., 1993. Conductivity discontinuities in the upper mantle beneath a stable craton, *Geophys. Res. Lett.,* **20,** 2941–2944.

Schultz, A. & Zhang, T.S., 1994. Regularized spherical harmonic analysis and the 3D electromagnetic response of the Earth, *Geophys. J. Int.,* **116,** 141–156.

Schultz, A. & Pritchard, G., 1999. A three-dimensional inversion for large-scale structure in a spherical domain, in '*ThreeDimensional Electromagnetics*', Vol. 7, pp. 451–476, eds Spies, B. & Oristaglio, M., Society of Exploration Geophysicists, *Geophysical Developments Series*.

Shankland, T.J. & Duba, 1990. Standard electrical conductivity of isotropic, homogeneous olivine in the temperature range 1200°–1500°C, *Geophys. J. Int.,* **103,** 25–31.

Shankland, T.J., Peyronneau, J. & Poirier, J.P., 1993. Electrical Conductivity of the Earth's lower mantle, *Nature,* **366,** 453–455.

Slepian, D., 1978. Prolate spheroidal wavefunctions, Fourier analysis, and uncertainly, V. Discrete case, *Bell. Syst. Tech. J.,* **57,** 1371–1429.

Svalgaard, L., 1975. Geomagnetic responses to the solar wind and to solar activity, *NASA Report SP366,* 119–142.

Thomson, D.J., 1977. Spectrum estimation techniques for characterization and development of WT4 waveguide, I, *Bell. Syst. Tech. J.,* **56,** 1769–1815.

Thomson, D.J., 1982. Spectrum estimation and harmonic analysis, *Proc. IEEE,* **70,** 1055–1096.

Thomson, D.J. & Chave, A.D., 1991. Jackknifed error estimates for spectra, coherences, and transfer functions, in *Advances in Spectrum Analysis and Array Processing,* Vol. 1, pp. 58–113, ed. Haykin, S., Prentice Hall.

Toh, H., Schultz, A. & Uyeshima, M., Geoelectromagnetic induction in a heterogeneous sphere: a stabilized biconjugate gradient solution and its acceleration over multiple frequencies, *Geophys. J. Int.,* submitted.

Uyeshima, M. & Schultz, A., 2000. Geoelectromagnetic induction in a heterogeneous sphere: a new 3D forward solver using a staggered-grid integral formulation, *Geophys. J. Int.,* **140,** 636–650.

Van Heijst, J.H. & Woodhouse, J., 1999. Global high-resolution phase velocity distributions of overtone and fundamental-mode surface waves determined by mode branch stripping, *Geophys. J. Int.,* **137,** 601–620.

Wallace, J.M. & Dickinson, R.E., 1972. Empirical orthogonal representation of time series in the frequency domain. Part I: Theoretical considerations, *J. Applied Meteol.,* **11,** 887–892.

Zhang, T.S. & Schultz, A., 1990. Exorcise-an algorithm for detection of spurious values and prediction of missing data, *Computers in Geosciences,* **16,** 1027–1065.

Zhang, T.S. & Schultz, A., 1992. A 3D perturbation solution for the EM induction problem in a spherical earth-the forward problem, *Geophys. J. Int.,* **111,** 319–334.